IOWA STATE UNIVERSITY
Digital Repository

1996

An FMCW radar system for short range surface contour mapping

Annette Lynn Latwesen
Iowa State University

Follow this and additional works at: http://lib.dr.iastate.edu/rtd

Part of the Electrical and Electronics Commons, Environmental Monitoring Commons, Mechanical Engineering Commons, and the Remote Sensing Commons

INFORMATION TO USERS

An FMCW radar system for short range surface contour mapping

by

Annette Lynn Latwesen

A dissertation submitted to the graduate faculty

in partial fulfillment of the requirements for the degree of

DOCTOR OF PHILOSOPHY

Major: Mechanical Engineering

Major Professors: Robert C. Brown and Robert J. Weber

Iowa State University

Ames, Iowa

1996

UMI Number: 9712574

UMI
300 North Zeeb Road
Ann Arbor, MI 48103

ii

Graduate College

Iowa State University

This is to certify that the doctoral dissertation of

Annette Lynn Latwesen

has met the dissertation requirements of Iowa State University

Signature was redacted for privacy.

Co-major Professor

Signature was redacted for privacy.

Co-major Professor

Signature was redacted for privacy.

For the Major Program

Signature was redacted for privacy.

For the Graduate College

TABLE OF CONTENTS

1 INTRODUCTION

The purpose of this research was to implement and evaluate an imaging system for monitoring the surface of a fluidized bed combustor (FBC). A fluidized bed combustor is a method for generating power and producing steam by burning coal and other low grade, variable quality fuels [12, 15]. Problems can occur within the bed of the combustor that will influence the performance of the FBC. As an example, under suitable conditions, the fine bed particles will cohere, forming agglomerates [20]. Agglomerates can undesirably affect the hydrodynamics and heat transfer characteristics of the FBC, and as the clusters increase in size, the large particles can defluidize the bed, resulting in combustor shutdown. Shutdowns are not only inefficient and costly, but also harmful to the combustor structure because of the additional wear due to thermal cycling.

Surface behavior reveals information about the dynamics of the bed material below the surface; for instance, stagnant regions may indicate the presence of an agglomerate or a plugged port in the distributor plate. A continuously updated image of the bed surface could be a valuable diagnostic tool for an operator of the combustor. In addition, an accurate image could be beneficial as an academic tool to verify models of FBC fluid dynamic processes. In recent years, several efforts have been made to monitor the circulation patterns in fluidized beds. However, a satisfactory system, capable of operating in real-time on a full scale fluidized bed, has yet to be developed.

For this project, a phased-array, frequency modulated continuous wave (FMCW) radar system was designed, developed, and evaluated. The testing of this 'proof-of-concept' system was limited to static, simple surfaces composed of sand or metallic objects. To upgrade the system so that it images the dynamic surface of an operational combustor, the imaging algorithms could be optimized for speed and modified to account for surface velocity changes, and, in addition, the system hardened for operation in a harsh environment.

2 BEAMFORMING WITH FMCW SIGNALS

This chapter reviews the properties and processing of FMCW radar signals to provide a better understanding of the detection and analysis methods of systems designed with FMCW radar sources. Before considering FMCW signals and their processing, a review of previous fluidized bed imaging systems and related radar-based surface mapping methods is provided. This is followed by a section describing the delay and sum beamforming algorithm. The chapter concludes with a section that summarizes the characteristics of FMCW signals and also provides guidelines for processing FMCW signals with the delay and sum beamformer.

2.1 Background

In general, a fluidized bed is a bed of fine particles placed on top of a perforated distributor plate. An air stream, or other fluidizing medium, enters via the distributor plate and flows vertically through the bed material. Fluidization occurs when the velocity of the air stream is large enough such that the weight of the particles is counterbalanced by the upward force exerted on the particles by the gas. (The term fluidization is applied because the properties and behaviors of the bed material while in suspension are similar to that of a fluid.)

Most of the efforts of imaging fluidized beds have been led by researchers at the Department of Energy's Morgantown Energy Technology Center (METC). One type of monitoring system developed and tested was a three-dimensional capacitive imaging system for mapping the density profile within the bed [5]. This system placed four sets of thirty-two electrodes along the inner surface of a 15.24 cm diameter polyvinyl chloride vessel containing a bed of irregularly shaped plastic beads. Each of the four imaging levels generated a cross sectional density map of the bed. When stacked, the images provided a three dimensional view of the bed. Although this system was capable of providing a three dimensional bed

profile, the set-up would be too unwieldly and insecure to function on a full scale, operational fluidized bed, and is most likely limited to laboratory-scale fluidized bed testing.

An alternative fluidized bed monitoring system, also designed and tested at METC, was an ultrasonic-based surface contour mapping system [6]. Noninvasive methods, such as this, are preferred since the sensors are not in contact with the fluidized bed and, therefore, less prone to damage. However, the combustion chamber of a fluidized bed reactor is a hostile environment that has high temperatures, ranging from 1200° to 1500° F, and harsh combustion gases, containing tar and corrosive compounds. Under these conditions, an ultrasonic system may not be appropriate since its performance can be affected by flying debris, buildup on sensor heads, and density changes in the gas above the bed surface [28].

An attractive choice for mapping the surface of an operational fluidized bed combustor is a microwave radar device. The microwave signals that probe the bed surface are less affected by atmospheric variations and would likely penetrate buildup on the sensors [28]. Furthermore, a radar system can be assembled completely external to the combustion chamber. The antennas could be mounted on the external wall of the combustion chamber, and a window, composed of a dielectric material capable of withstanding the combustion chamber environment and transparent to the radar signals, would separate and protect each antenna from the hazardous conditions of the combustion chamber. Depending on the length of cables connecting the radar transmitter and receiver to an antenna pair, the data acquisition and analysis equipment can be remotely located from the combustor.

Many radar-based surface imaging methods are variations of synthetic aperture radar (SAR), which was first introduced in the 1950s [2]. Since then, SAR has become a well-known method for producing high resolution images of terrain and ocean surfaces. [10, 13, 25]. SAR is typically a long range imaging system that is associated with a moving antenna, transported by an airplane or a satellite, and a stationary target. As the antenna moves along the flight path, the radar system transmits pulses towards a surface area and receives echos from the same area. The phrase 'synthetic array' describes the transmit/receive properties of the antenna at discrete spatial locations as it travels with the satellite or airplane.

Instead of providing a contour map of surface elevations, SAR generates a high resolution map of the radar reflectance properties of the surface. However, the images describe the surface profile, since patterns in the reflectance map will be primarily caused by variations in the surface roughness if the dielectric properties of the surface are uniform [27].

With coherent processing of the received signals and proper SAR system design, high resolution in both cross-range and range dimensions is achievable. Cross-range resolution improves as the array is enlarged; whereas, range resolution becomes better as the bandwidth of the transmitted signal is increased [3, 17]. For imaging the surface of a fluidized bed, which may have a diameter of only a couple meters, a SAR system requires a wide bandwidth radar source. As an example, to provide 6 in. range resolution, a radar source with a bandwidth of 1 GHz would be necessary [2]. If a short range (high resolution) imaging system is limited to moderate bandwidth radar sources, poor range resolution would deem an SAR approach unacceptable.

Surface topography has also been measured by mounting radar altimeters on satellites or airplanes. By measuring the time delay between transmitting a pulse of energy and receiving the reflection from the earth's surface, the distance to the surface can be estimated. If the radar altimeter employs frequency modulation, the frequency shift of the returned signal determines the distance to the earth's surface. In either case, the signal is transmitted at normal incidence to the surface so that when reflected, the signal is received at the radar. As the satellite or airplane travels aboves the surface, a map of the surface contour is produced. The collection of articles presented in [27] provides an overview of microwave imaging systems including SAR and radar altimetry.

This project designed a short range microwave imaging system based on principles of radar altimetry rather than SAR. A planar antenna array mounted less than 10 ft. above a test surface scanned a beam of energy across the surface. The scanning process was performed off-line with the delay and sum beamforming algorithm. By applying the ranging properties of the frequency-modulated radar source, distances to each illuminated region of the surface were estimated and a map of the surface topography was created.

2.2 Delay and Sum Beamforming

A single antenna usually radiates a relatively wide beam of energy, and consequently, offers low directivity and poor spatial discrimination [1]. Its radiation field pattern is determined by the size and shape of its aperture. As the dimensions of the antenna aperture are enlarged, the beamwidth decreases and directivity improves. In many applications, rather than manufacture a large antenna, it is more practical to use multiple elements (an antenna array) to achieve a desired radiation pattern.

The radiation pattern of an antenna array is controlled by the dimensions of the overall array, the geometrical configuration of the array (linear, circular, rectangular, cylindrical, etc.), and the excitation phase and amplitude of each element [11]. The first two controlling properties, size and layout, determine the general shape of the beam. The amplitude distribution used to excite the elements of the array affects the beamwidth and sidelobe levels of the energy pattern, and the phase distribution directs, or steers, the beam. Manipulating the amplitude and phase distributions to accentuate radiation energy in some directions and suppress it in others is called beamforming.

Beamforming is a essentially the process of applying a spatial filter to signals received by an antenna array [4, 26]. The passband and stopband properties of the spatial filter are defined by the steered radiation pattern. Although it is convenient to view beamforming as an operation on received signals, beamforming is applicable to either transmission or reception of energy [26].

It is worth noting that the processing of waveforms sampled in space draws many parallels to the processing of signals sampled in time. As a result, many established spectral analysis techniques have been repackaged as array processing methods. Although the delay and sum beamformer is presented below (a Fourier transform based approach), various 'high resolution' beamformer strategies (cf. multiple signal classification [9], maximum entropy method, and autoregressive modeling [7]) have time domain counterparts. Like their time-domain cousins, these high resolution methods are not robust; to be effective they require an accurate model of the field, adequate signal-to-noise ratio, and statistically stable estimates of the sensor covariance matrix [24].

Because of its ease of implementation and robust nature, the delay and sum algorithm is the most popular beamforming method [11]. The general idea is to adjust the phase of each sensor output so that when the signals are summed, waveforms from a desired direction add together constructively, while interference from noise and other waveforms is reduced. The phase adjustment is based on the location of the sensor, the "look" direction, and the diffraction region that the waveform's source is located.

If a target is in the far field of an antenna array, then the reflected field approximates a uniform plane wave across the dimensions of the array [14]. As such, the value of the signal along a line, or plane, perpendicular to the direction of propagation is constant. Consider a plane wave impinging on a linear array as depicted in Figure 2.1. The value of the spatially sampled wavefield, $y_m(t)$, at time t, and any sensor location, $\vec{r}_m$, may be written [11]

$$
\begin{aligned}
y_m(t) &= s(\omega t - \vec{k}_0 \cdot \vec{r}_m) \\
&= s(\omega t + k|\vec{r}_m|\sin\theta_0)
\end{aligned}
\tag{2.1}
$$

where the wave vector, $\vec{k}_0$, defines the angle of incidence, θ_0, and has a magnitude equal to the wavenumber, and ω denotes the radian frequency of the propagating signal. The wavenumber is related to the wavelength of the signal by
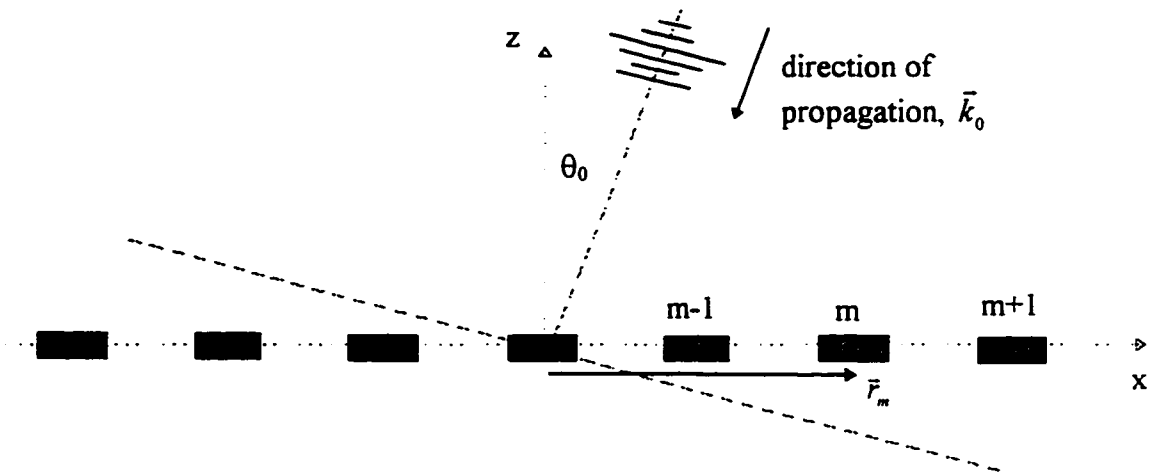
$$
k = \frac{2\pi}{\lambda}.
\tag{2.2}
$$

Figure 2.1 Plane waves impinging on a linear array.

As described by Eqn. 2.1, when the waveform propagates across the array, the signals received by sensor m-1 are a delayed version of the signal received by sensor m. (Assuming that no noise or other waveforms are present.)

The intent of the delay and sum beamformer is to introduce signal processing delays into each received signal to align the waveforms at the surface of array. When summed, the signals that are arriving from an angle θ_0 and captured by the array will add together constructively.

For an array having M sensors, the general expression for the output signal of the delay and sum beamformer is

$$z(t) = \sum_{m=0}^{M-1} w_m s(\omega t - \vec{k}_0 \cdot \vec{r}_m + \Delta_m).$$

(2.3)

w_m is a weight applied to the signal received by sensor m, and forms an amplitude distribution across the array. For a uniform array, all weights are unity. If the phase delay is selected as

$$\Delta_m = \vec{k}_0 \cdot \vec{r}_m$$

(2.4)

to oppose the propagation delays, the beamformer "stacks" the signals propagating from direction θ_0 so that they reinforce each other (Figure 2.2) while reducing the influence of signals propagating from other directions.
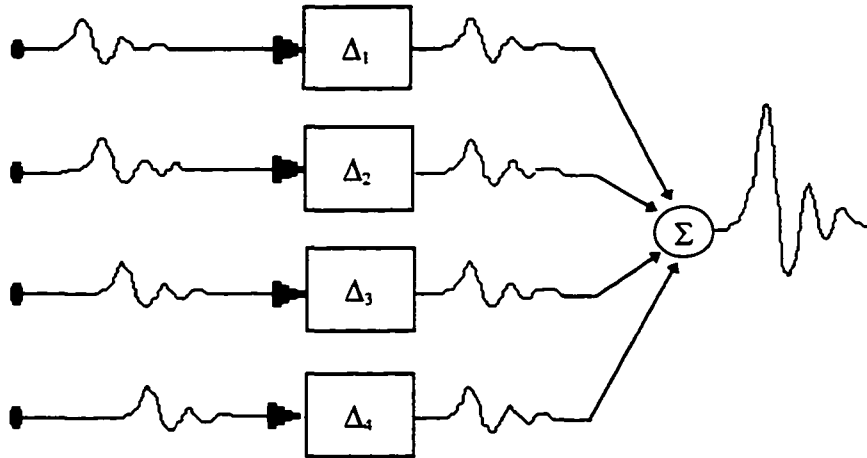
Figure 2.2 Stacking signals received from a desired direction. [10]

To verify that the far field beamformer expression is applicable, the phase difference of the scattered field across the array must be acceptable. Ideally, for a target placed along the center axis of the array, the scattered far field should arrive in-phase at all points on the surface of the array. However, if the target is in the near field, rather than far field, of the antenna array, the field at the array will have a spherical phase front, and the fields arriving at the edge of the array will be retarded in phase from those arriving at the center of the array because of the larger distance traveled. The general requirement for the target to be located in the far field is that the additional distance traveled cannot be greater than a fraction of the wavelength [16]. As an approximation, the path length difference should be less than $\lambda/16$. However, this value is only a guideline, and depends on the tolerance necessary.

If the scatterer is in the near field, the delay and sum beamformer must align the received signals from a target along a spherical surface. Figure 2.3 shows a spherical wave propagating towards a linear array. In this case, the sampled wavefield has the form [11]

$$y_m(t) = \frac{1}{|\vec{r}_m^0|} s(\omega t - k|\vec{r}_m^0|)$$ (2.5)

where $|\vec{r}_m^0|$ is the distance from the target to element m of the array. The coefficient in Eqn. (2.5) accounts for attenuation as the wave travels. (This term was not included in the far field source signal, Eqn. (2.1), because as plane waves, the array could not deduce the range to the source. On the other hand, the near field beamformer focuses the array on a specific spatial location.) If the phase of the near field delay and sum beamformer is chosen as

$$\Delta_m = k(|\vec{r}_m^0| - |\vec{r}^0|),$$ (2.6)

the output of the beamformer becomes

$$z(t) = \sum_{m=0}^{M-1} w_m s(\omega t - k|\vec{r}_m^0| + \Delta_m) / |\vec{r}_m^0|$$

$$= \frac{1}{|\vec{r}^0|} s(\omega t - k|\vec{r}^0|) \sum_{m=0}^{M-1} w_m \frac{|\vec{r}^0|}{|\vec{r}_m^0|}$$ (2.7)

Indeed, the beamformer reproduces the signal received at the center of the array, multiplied by a weighting factor.

The path length adjustment, $\left|\vec{r}^0\right| - \left|\vec{r}_m^0\right|$, written in terms of the direction of wave propagation and element locations is a simple calculation based on the Law of Cosines:

$$\left|\vec{r}_m^0\right| = \left[\left|\vec{r}^0\right|^2 + \left|\vec{r}_m\right|^2 - 2\left|\vec{r}^0\right|\left|\vec{r}_m\right|\cos\psi\right]^{\frac{1}{2}}$$

$$\left|\vec{r}_m^0\right| = \left|\vec{r}^0\right|\left[1 + \frac{\left|\vec{r}_m\right|^2}{\left|\vec{r}^0\right|^2} - \frac{2\vec{r}^0 \cdot \vec{r}_m}{\left|\vec{r}^0\right|^2}\right]^{\frac{1}{2}}$$

$$\left|\vec{r}^0\right| - \left|\vec{r}_m^0\right| = \left|\vec{r}^0\right|\left(1 - \left[1 + \frac{\left|\vec{r}_m\right|^2}{\left|\vec{r}^0\right|^2} - \frac{2\vec{r}^0 \cdot \vec{r}_m}{\left|\vec{r}^0\right|^2}\right]^{\frac{1}{2}}\right) \qquad (2.8)$$
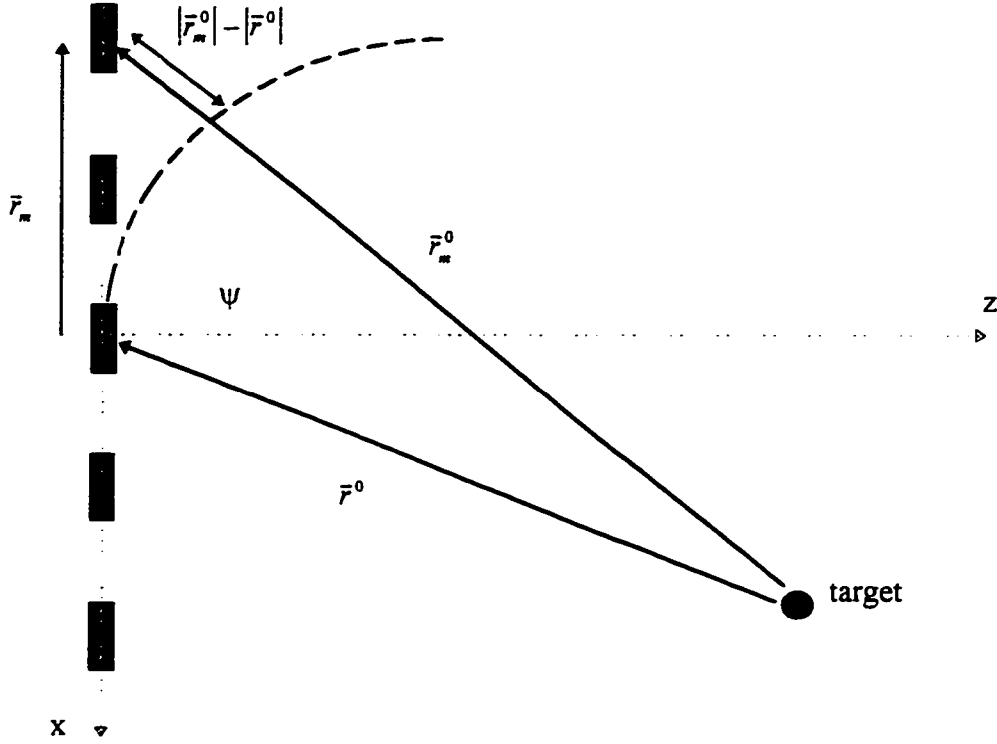

Figure 2.3 A linear array in the near field of a scatterer.

For some targeting systems, the location of the scatterer is determined by varying $|\bar{r}_0|$, the distance to the scatterer, until the integrated output of the beamformer is maximized [11]. Thus, for each look direction, the beamformer's output is computed for several target ranges as it hunts for the true location. When mapping a real time image of a surface, this approach would likely be too time-consuming. However, it may be sufficient to approximate $|\bar{r}_0|$ if other characteristics of the signal, such as frequency, provide target location.

In some imaging cases where the array is in the near field of the surface scatterers, it may be adequate to focus the array on a plane positioned at an average surface level, especially if real time processing is necessary and the induced phased errors are minor. Figure 2.4 displays a target located in the near field of an antenna array, and a false target positioned on a plane at a different distance from the array. Previously it was mentioned that the phase difference across a planar array was acceptable if phase fronts did not differ by more than $\lambda/16$. A similar criterion applies here. Namely, that focusing the array on the false target yields acceptable results if the value of the beamformer path length correction $|\bar{r}^0| - |\bar{r}_m^0|$ does not differ by more than $\lambda/16$ from the value of the beamformer path length correction when focused on the true target, $|\bar{r}^0| - |\bar{r}_m^0|$. More succinctly,

$$\left| \left(|\bar{r}^0| - |\bar{r}_m^0| \right) - \left(|\bar{r}^0{}'| - |\bar{r}_m^0{}'| \right) \right| < \frac{\lambda}{16} \qquad (2.9)$$

By focusing the beamformer on a plane, located at an average distance to the surface, only one beamformer output calculation is required at each look direction. Thus, the imaging algorithm has the speed of a far field beamformer, yet, the phase adjustments (slightly compromised) of a near field beamformer.

All of the previous beamforming equations were defined for an array either transmitting or receiving energy. If the array operates as both a transmitter and a receiver, the total phase delay added to the received signal must account for the phase shift applied to the transmitted signal. Therefore, the phase delay depends on the location of the array element that received the scattered signal as well as the location of the element that transmitted the

pulse. (Signals must be recorded for each transmitter/receiver pair of the antenna array.) The output of the far field beamformer becomes

$$z(t) = \sum_{\alpha=0}^{M-1}\sum_{rx=0}^{M-1} w_\alpha w_{rx} s(\omega t - \phi + \Delta_{\alpha,rx})$$

$$\Delta_{\alpha,rx} = \Delta_\alpha + \Delta_{rx} \qquad\qquad (2.10)$$

$$= \vec{k}_0 \cdot \vec{r}_\alpha + \vec{k}_0 \cdot \vec{r}_{rx}$$

where ϕ represents the phase of the received signal, $\Delta_{\alpha,rx}$ is the additional phase delay introduced by the beamformer, and $\vec{k}_0$ defines the direction that the array is steered. A similar modification can be made to the phase delay of the near field beamformer.

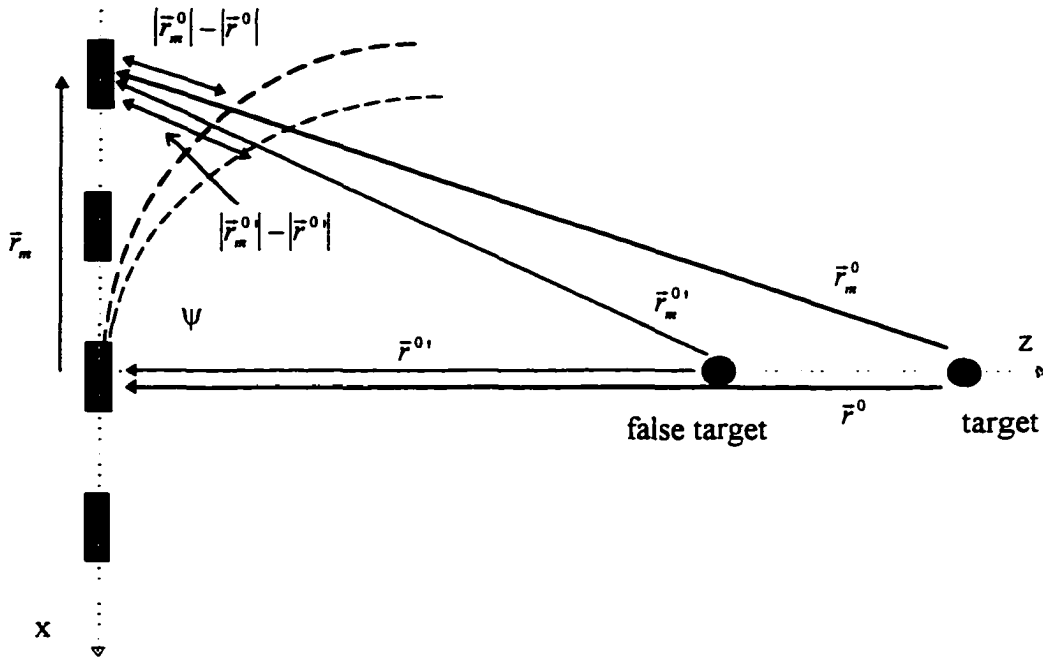Figure 2.4 Focusing the array on a false target located at an average surface level

2.3 Frequency Modulated Continuous Wave (FMCW) Radar

The theory of FMCW radars is well established [19, 22]. Included here is a basic analysis of the behavior of linear FMCW radar. The analysis is for a single target traveling in a homogeous medium; however, because the system is linear, the extension to multiple targets

is a straightforward application of superposition. The analysis also assumes that the target is stationary. (For an analysis that accounts for moving targets see [22].)

Before carrying out the analysis, it may be useful to define the concepts of instantaneous angular frequency and instantaneous phase. When the frequency of a sinusoidal signal is time varying, the signal's phase characteristics are described by either of these two quantities [23]. The definitions of both are interrelated:

instantaneous phase, $\theta(t) = \int_0^t \omega(\tau)d\tau + \theta_0$ (2.11)

instantaneous angular frequency, $\omega(t) = \dfrac{d\theta}{dt}$.   (2.12)

As a simple example, consider a sinusoid with a constant angular frequency, ω_0. By definition, the phase of the signal progresses linearly in time as $\omega_0 t + \theta_0$, with the frequency of the sinusoid represented by ω_0.

Linear FMCW radar sweeps a carrier frequency over a band of frequencies, ranging from f_0 to f_1, during a sweep period, T. This is graphically displayed in Figure 2.5. The transmitted signal has the form

$$s(t) = a_s \sin\left[2\pi\left(f_0 t + \frac{\alpha t^2}{2}\right)\right] rect\left(\frac{t}{T}\right)$$ (2.13)

where α represents the frequency sweep rate (chirp rate), a_s is a constant representing the peak magnitude of the signal, and *rect* is the rectangular windowing function (or gate function). This signal reflects off a single target at a distance R, and is received a short time later as an attenuated version of the transmitted signal:

$$y(t) = a_y \sin\left[2\pi\left(f_0(t - \tau_d) + \frac{1}{2}\alpha(t - \tau_d)^2\right)\right] rect\left[\frac{(t - \tau_d)}{T}\right].$$ (2.14)

The amount of time taken to travel to the target and return is represented by the time delay

$$\tau_d = \frac{2R}{c}$$ (2.15)

where c is the velocity of propagation in the medium carrying the signal. Note that the instantaneous frequency of the received signal is

$$\omega(t) = 2\pi\left[f_0 + \alpha t - \alpha \tau_d\right],$$
(2.16)

which differs from the frequency of the transmitted signal at any instance in time, by $\alpha\tau_d$. This is also illustrated in Figure 2.5.
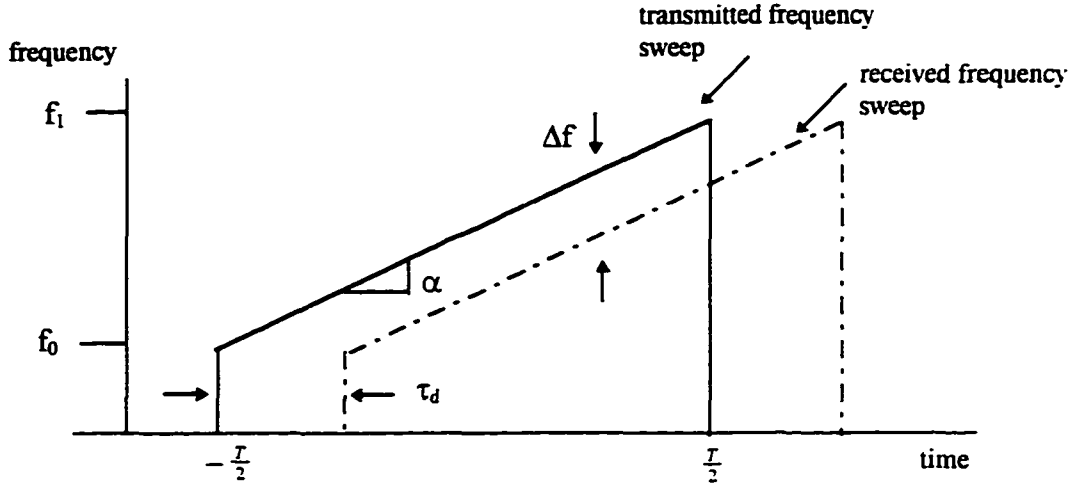

Figure 2.5 The frequency characteristics of an FMCW signal

After the signal is reflected and received, it is multiplied with a replica of the transmitted signal and processed with a low-pass filter. The result is a constant frequency signal

$$x(t) = a_x \cos\left[2\pi\left(\alpha\tau_d t + (f_0 - \frac{\alpha\tau_d}{2})\tau_d\right)\right] rect\left[\frac{(t - \tau_d)}{T}\right].$$
(2.17)

The frequency of the demodulated signal is proportional to the round trip propagation delay, and, hence, carries range information. If the demodulated echo signal has a frequency, f_y, then the range to the target is simply

$$R = \frac{cf_y}{2\alpha}.$$
(2.18)

In the event that multiple targets are present, the total return signal is the sum of all the reflected signals, which are replicas of the transmitted signal but delayed by various amounts. Thus, the demodulated signal is a collection of sinusoidal signals having different frequencies.

When steering distances (path length corrections), δ, are added to the round trip distance traveled by the signal, the demodulated echo takes the form

$$x_s(t) = a_x \cos\left[2\pi\left(\alpha(\frac{2R+\delta}{c})t + f_0(\frac{2R+\delta}{c}) - \frac{\alpha}{2}(\frac{2R+\delta}{c})^2\right)\right]. \qquad (2.19)$$

(The rectangular windowing function has been removed from the equation, but is implied.) After expanding and regrouping terms, the signal becomes

$$x_s(t) = a_x \cos\left[2\pi\left(\alpha\tau_R t + (f_0 - \frac{\alpha\tau_R}{2})\tau_R + \alpha\tau_s t + (f_0 - \frac{\alpha\tau_s}{2})\tau_s - \alpha\tau_R\tau_s\right)\right] \qquad (2.20)$$

where $\tau_R = \dfrac{2R}{c}$ is the time delay between the transmitted and received signals, and

$\tau_s = \dfrac{\delta}{c}$ is the additional time delay caused by steering the array. Applying a trigonometric

identity to Eqn. (2.20) results in an equation of the form

$$x(t) = \cos(\beta t + \theta)\cos(\varepsilon t + \phi) - \sin(\beta t + \theta)\sin(\varepsilon t + \phi) \qquad (2.21)$$

with

$$\beta = 2\pi\alpha\tau_R$$

$$\theta = 2\pi\left(f_0 - \frac{\alpha\tau_R}{2}\right)\tau_R$$

$$\varepsilon = 2\pi\alpha\tau_s$$

$$\phi = 2\pi\left(f_0\tau_s - \frac{\alpha\tau_s^2}{2} - \alpha\tau_R\tau_s\right)$$

The form of Eqn. (2.21) is intriguing because the expressions $\cos(\beta t + \theta)$ and $\sin(\beta t + \theta)$ are measurable quantities, and indeed, are the demodulated echo signal and its quadrature (see Eqn. (2.17)). In addition, since the last two terms in the expression for ϕ are secondary terms and are negligible compared to the initial term, all of the terms in the remaining two sinusoidal expressions are determinable from properties of the FMCW radar source and estimated steering delays.

Eqn. (2.21) contains the necessary delays to steer an array element, radiating a linear FMCW signal, towards a region on the surface. When substituted into Eqn. (2.10) for s(·), Eqn. (2.21) becomes the basis of the linear FMCW, phased-array imaging algorithm.

3 EXPERIMENTAL APPARATUS

The purpose of this project was to determine the feasibility of a short range phased-array imaging system. To pursue this task, a prototype system was developed to image various 4 ft. × 4 ft. surfaces placed, on average, 7.8 ft from an antenna array. This chapter describes the equipment arrangement and signal processing procedures implemented for the system.

A block diagram of the equipment set-up is shown in Figure 3.1. Each item in the diagram is described in detail below.

The test target for all imaging experiments was a 4 ft. × 4 ft. bed of sand, 1.5 ft. deep, contained in a plywood box. A wooden mounting structure placed an antenna array above the bed (Figure 3.1). The distance from the bottom of the bed to the array could vary from 7.5 ft. to 9 ft. with 0.5 ft. increments. To reduce reflections from the floor beneath the bed, water was added to the sand, which would absorb some of the energy traveling through the bed [18]. Enough water was added so that the bottom 6 in. of sand was damp, but not saturated, whereas the top layer was dry to slightly damp. An $\frac{1}{8}$ in. thick plastic sheet protected the plywood box from the wet sand. In addition, a second layer of plastic covered the bottom 6 in. of sand so that it would retain its moisture.

It was determined experimentally that the low reflectivity of the pure sand surface was influencing the performance of the microwave imaging system. Because only a small portion of the transmitted signal was reflected by the dielectric interface, the typical return was characterized by unwanted signals (leakage signals, returns from the plywood sheet beneath the sand bed, and other noise signals). As a result, the images of sand surfaces produced by the radar system were of poor quality. To improve the reflective nature of the sand surface, it
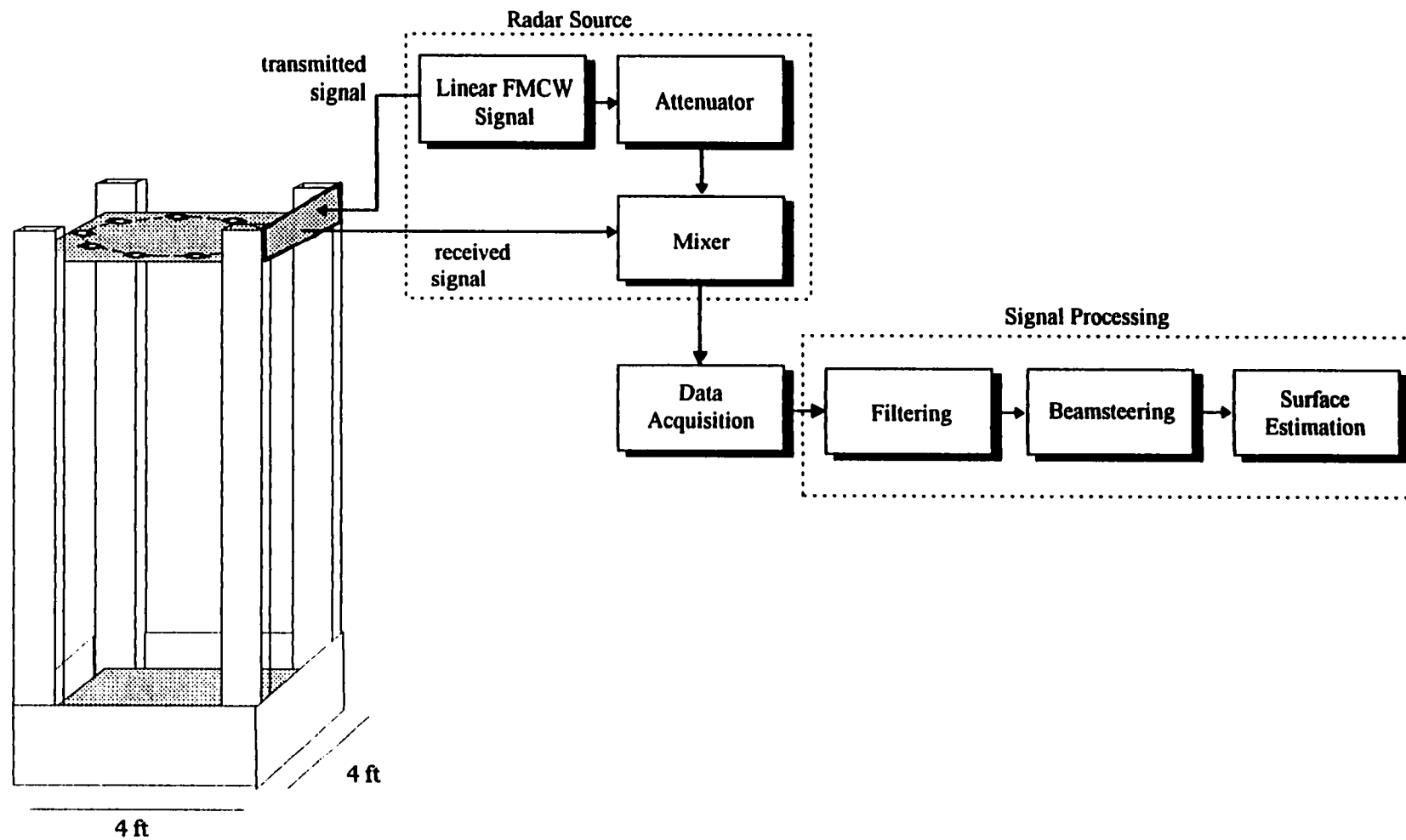
Figure 3.1 The short range radar imaging system

was covered with randomly dispersed pieces of aluminum foil (ranging in size from 4 in^2 to 16 in^2). Approximately 40% of the surface area was covered with foil. This sort of surface was a compromise between a sand surface and a continuous metal sheet. The surface responded better than pure sand, and took the contour of the sand surface, yet was not as reflective as a large sheet of metal or foil. Since the pieces were rearranged on the surface quite often, the size of the pieces was selected to reduce surface set-up time.

Besides the modified sand surface, other surfaces that were imaged included a 3 ft × 3 ft. × $\frac{1}{4}$ in. sheet of aluminum and strips of foam board that were lined with continuous sheets of foil. Surfaces of these materials were constructed on top of the sand bed.

The antenna array was a nine element circular array with a 30 cm radius (Figure 3.2). Each element was a Hewlett Packard Model G281A rectangular adapter having a circular mounting flange. A cable connected each antenna to an antenna switchboard where the system operator manually connected a desired antenna pair to the transmitter and receiver cables of the radar system.
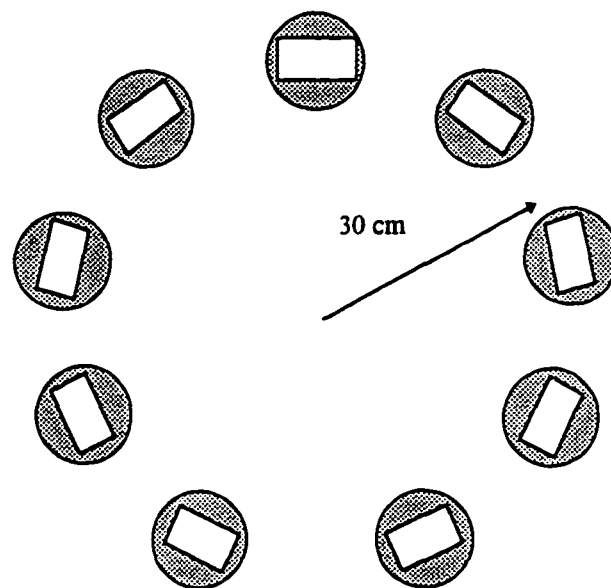
Figure 3.2 A 30 cm. circular antenna array

The small spacing between elements allowed considerable direct path crosstalk. To reduce leakage signals, baffles were placed partially around each antenna element and each element was oriented such that the main axis was tangential to a radial line. Although this did not eliminate the leakage signals, it did reduce them to about the same magnitude as the signals received as reflections from the surfaces. Without these efforts, the leakage signals could be as much as 20 times larger than surface reflections.

In a harsh environment, baffles would make the system awkward and undesirable. In this case, it is recommended that an antenna array composed of horn apertures be implemented. Antenna horns attached to the rectangular apertures were experimentally determined to almost eliminate leakage signals of a five element linear array having 14.5 cm interelement spacing. The 30 cm. array was too small to permit the use of antenna horns, and due to limited funding, a set of nine horns was not purchased for this project.

The radiation power pattern of the antenna array at the surface of the sand bed (7.5 ft from the array) is displayed in Figure 3.3. The pattern has a half-power beamwidth of 4.5 in. and sidelobes, -15 dB relative to the mainlobe, encircling the beam at a 2 ft. radius. The radiation pattern is derived in Appendix A.
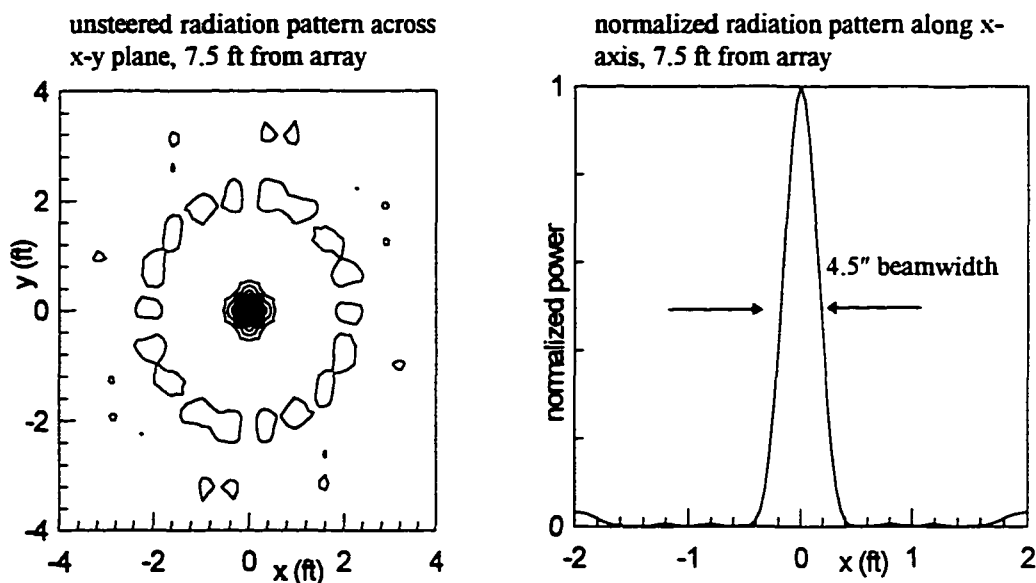

Figure 3.3 Radiation power pattern of 30 cm circular array

The radar source was a Rockwell 55-A altimeter, which produced a triangular FMCW signal having a 4.3 GHz center frequency and 100 MHz sweep frequency. The output power was 350 mW. The purchased altimeter had a modulation frequency of 100 Hz.

With a 100 MHz bandwidth, the frequency-to-range conversion was 40 Hz per foot. Several electronic components were replaced in the altimeter to change the modulation frequency to 1000 Hz and shift the conversion factor to 400 Hz per foot. This expanded the frequency range separating targets.

The radar system demodulated the received signal by mixing it with an attenuated copy of the transmitted signal. The demodulated signal was further conditioned with several stages of amplification and filtering before being sampled by the data acquisition system.

The data acquisition system was comprised of a 486 microprocessor operating with a 66 MHz clock, a UEIDAQ Win-30D data acquisition board, and an additional timing circuit for controlling the triggering of the data acquisition board. The Win-30D features 12 bit resolution on each of its 14 analog input channels, has three 8 bit digital ports, and can convert up to 1 million samples per second. The sampling rate, sampling period, and channel selection were adjustable options available from an interface written in Visual C++. Typically, the sampling rate was 200 kHz for a period of 0.5 ms (one upramp of the altimeter). Besides acquiring, storing, and displaying the collected data, the program digitally controlled two solid state switches that passed either in-phase or quadrature signals to the altimeter's receiver circuitry.

Thirty six unique transmitter/ receiver antenna pairs exist for a nine element array. With an in-phase and a quadrature signal recorded for each antenna pair, a complete data set consisted of 72 signals. After collecting the data, it was processed by the beamsteering algorithm to generate a map of the surface contour.

4 DATA ANALYSIS PROCEDURES

This chapter describes the stages in the signal processing procedure. The process of extracting a surface contour map from an acquired data set requires several steps. Foremost to the procedure is the beamsteering algorithm. However, prior to the beamsteering algorithm, the signals must be processed to reduce noise and prepare the signals for steering. As the beamsteering algorithm scans across the surface, the output of the beamsteering algorithm is analyzed to estimate the range to the surface at each direction of look. Finally, after an initial contour map of the surface is developed, the image is spatially filtered to smooth out areas affected by noise.

4.1 Noise Reduction

The procedure for processing the collected data sets is diagrammed in Figure 4.1. Aside from the beamsteering algorithm, most of the computationally intensive signal processing tasks in the imaging algorithm are devoted to noise removal. Although the delay and sum beamforming algorithm is fairly robust to noise, reducing noise levels enhances the image results. This is especially important for areas on the surface with low reflectivity, where noise signals can mask low power signals. Even in areas where the power return from the surface is relatively high, noise causes small variations in a surface estimate.

Many of the noise sources are not random disturbances, but rather, interference resulting from leakage, multipath, or radiation pattern sidelobes. Other more subtle noise sources include instrument bias, time varying instrument properties, and phase errors introduced by signal processing. By attenuating these noise signals prior to beamsteering, the accuracy of the surface reconstructions will certainly be improved.
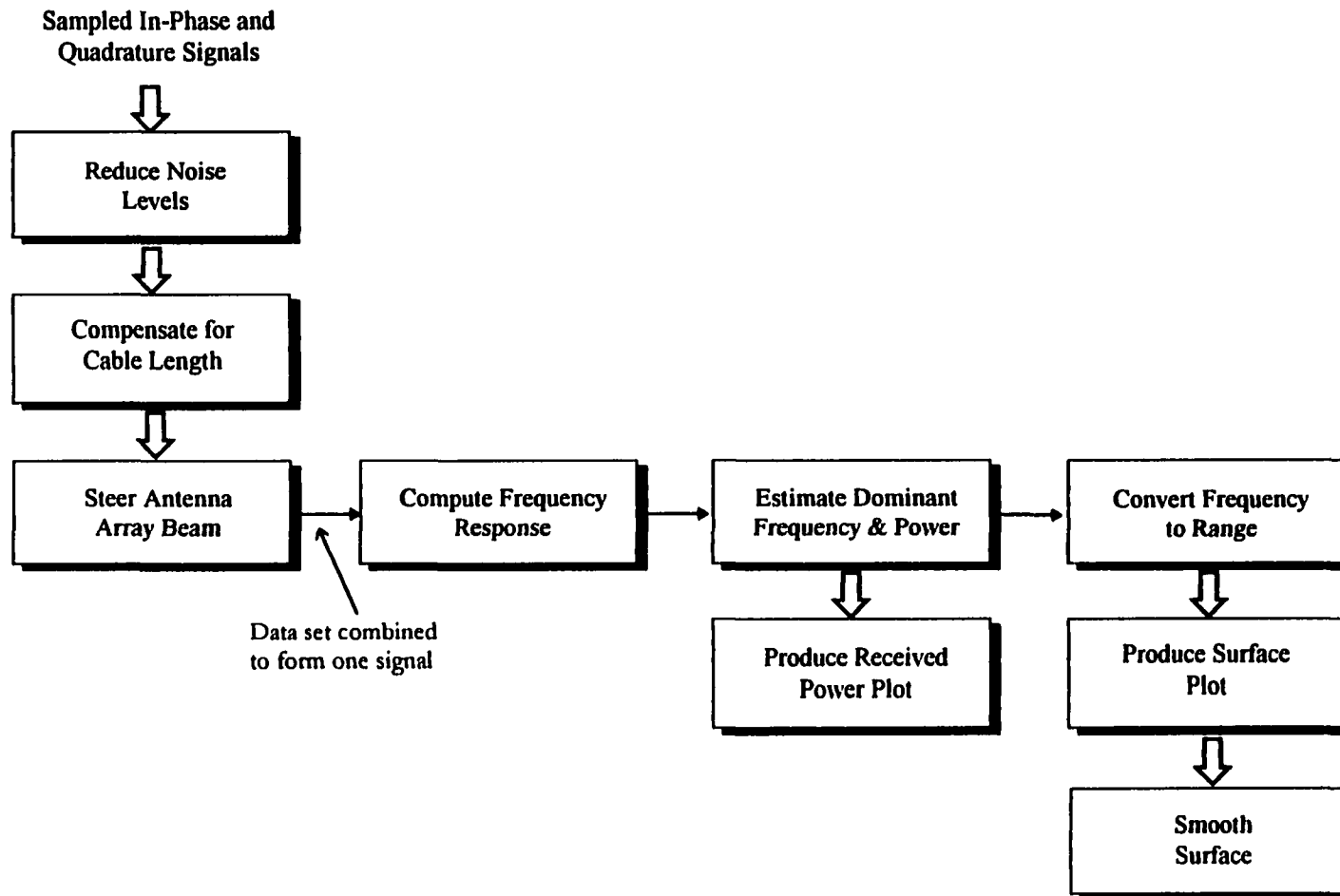
Sampled In-Phase and
Quadrature Signals

⇩

Reduce Noise
Levels

⇩

Compensate for
Cable Length

⇩

Steer Antenna
Array Beam → Compute Frequency
Response → Estimate Dominant
Frequency & Power → Convert Frequency
to Range

Data set combined
to form one signal

Produce Received
Power Plot

Produce Surface
Plot

⇩

Smooth
Surface

22

Figure 4.1 Signal Processing Steps

The only noise signal that is accessible "off-line" (that is, when a surface is not being probed) is a time-invariant interference produced in the receiver circuitry and measurable even when the transmitter cable is disconnected from the altimeter. The in-phase and quadrature components of this signal are shown in Figure 4.2. Since these components are not in-sync with one another, the signal is not confined to the receiver circuitry. At least part of the signal is produced by a wave traveling from the receiver towards the receiving antenna, where it is reflected, passed through the in-phase or quadrature switches, and received. Regardless of the cause, this low frequency bias signal interferes only slightly with the high frequency signals resulting from surface reflections. Nevertheless, the in-phase and quadrature components are measured before each imaging data set and subtracted from every received signal pair.
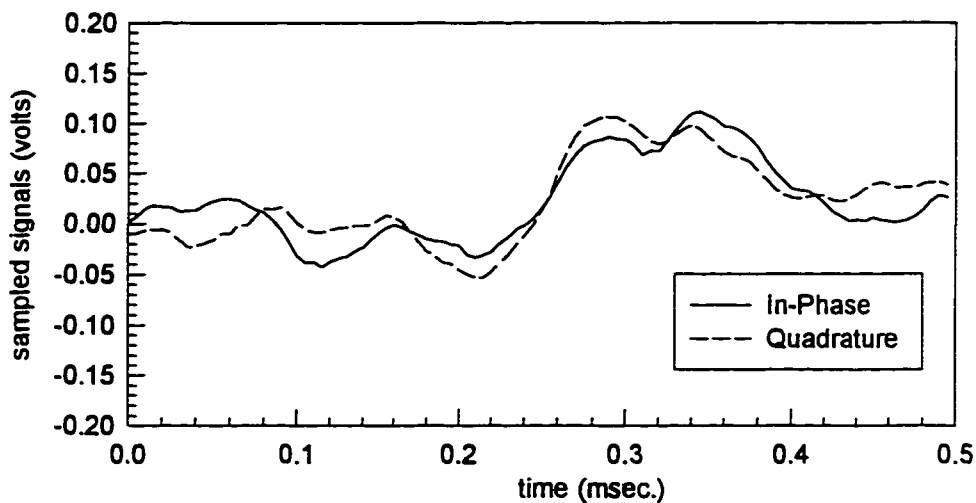

Figure 4.2 In-phase and quadrature components of receiver noise

Leakage signals are the largest source of noise in this imaging system. Several changes were made to the circular antenna array to reduce direct path crosstalk between antennas. Although these steps significantly reduced the leakage signals, a crosstalk signal remained a dominant constituent of most received signals.

One of the most effective methods for eliminating leakage signals was background subtraction. Using this approach, a background data set (a data set taken with a layer of five absorber pads placed on top of the sand surface) was subtracted from an image data set prior

to beamsteering. This is a simple but efficient way to eliminate any noise sources common to both background and image data sets. The drawback of this method is that it does not work well with sand surfaces or other surfaces with low reflectivity because the signals reflected by the (non-ideal) absorber material have magnitudes equivalent to the signals reflected by a low reflectivity surface. On one hand, by subtracting the background data set, the leakage signals are being removed, but on the other hand, additional interference signals (reflections from the absorber surface) are being introduced. To make matters worse, the signals reflected by the absorber pads have frequencies closely spaced to the surface reflections, and, thus, not resolvable in the frequency domain.

Several frequency responses are shown in Figure 4.3 for comparing results before and after applying background subtraction. The graphs indicate the relative strength of the signals received by the same antenna pair for different surface materials. All surfaces were flat. The signal reflected by the sand surface is the weakest, whereas the signal reflected by the metal sheet is the strongest. The frequency response of the leakage signal is represented in all curves prior to background subtraction by the peak centered at 19.6 kHz. After subtracting a background data set, the leakage signal is eliminated from the signals.

Another method for reducing interference signals was termed noise estimation and subtraction. This approach was taken when imaging sand surfaces and other surfaces with low reflectivity. With this approach, an estimate of the leakage signal is subtracted from the received signal. The estimated signal is sinusoidal with the same characteristics (magnitude, frequency, and phase) of the leakage signal, which are revealed by a signal's frequency spectrum. An advantage of this approach over direct bandpass filtering is that the sidelobes of the interfering signal, resulting from windowing, are also removed in the process. These sidelobes occur at about the same frequency as signal reflections from surfaces and would likely influence the imaging algorithm result.

The noise estimation and subtraction procedure is repeated for all acquired signals— both in-phase and quadrature—to reduce noise levels in the data. The method is also useful for removing a high frequency signal created by multipath. Figure 4.4 displays the results of

Frequency responses of acquired signals before applying
background subtraction
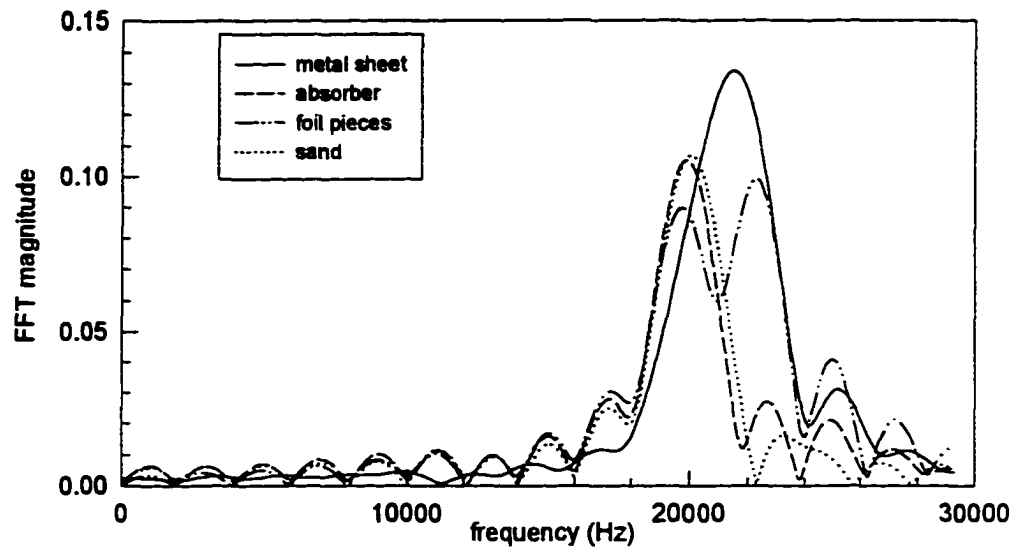
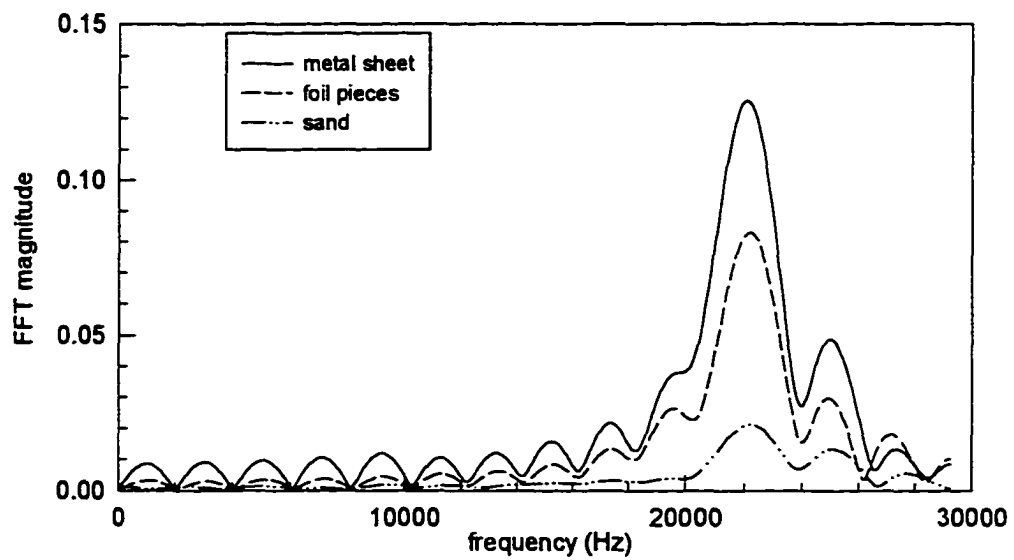Frequency responses after applying background subtraction

Figure 4.3 Frequency responses of acquired signals before and after applying background subtraction

applying noise estimation and subtraction to an acquired signal. To indicate the multipath signal, the estimated target ranges are marked in the figure.

In some cases, the frequency response of an acquired signal does not have well defined peaks distinguishing the leakage signal from the surface reflection (Figure 4.5). In such cases, the two signals cannot be separated, and the estimation and subtraction method will not perform as well as the background subtraction method, which would likely remove the noise signal.
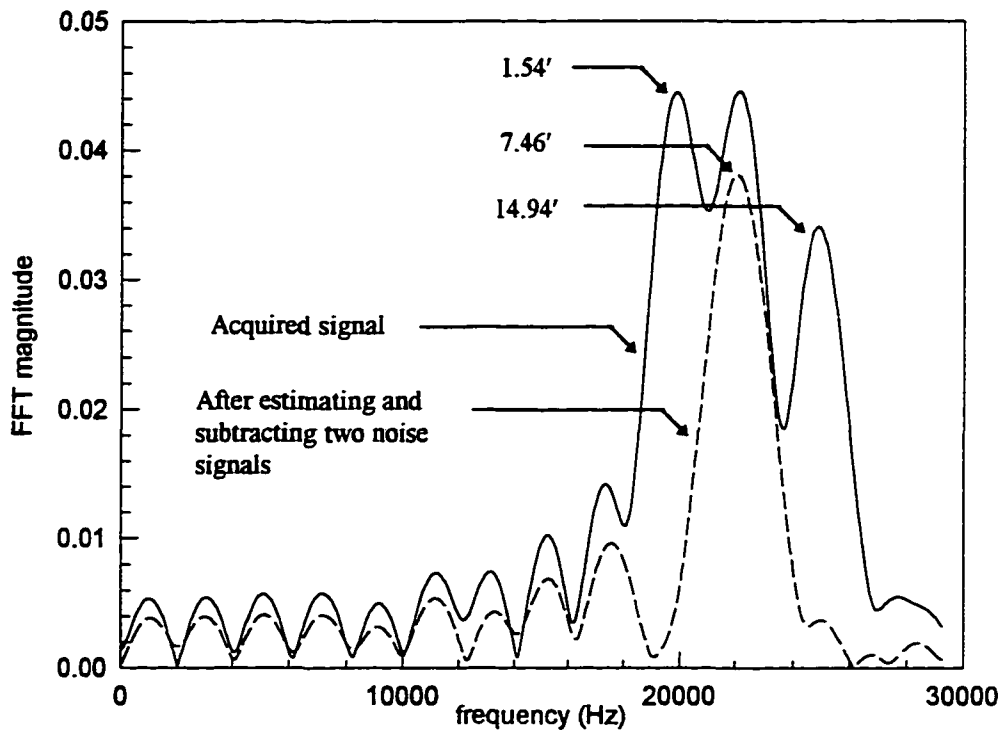

Figure 4.4 Demonstration of noise estimation and subtraction

Aside from removing a leakage signal and possibly a large multipath reflection, the collected signals were not filtered further because of the phase sensitivity of the beamsteering algorithm. Processing the signals prior to the beamsteering algorithm was kept to a minimum to reduce phase distortion.
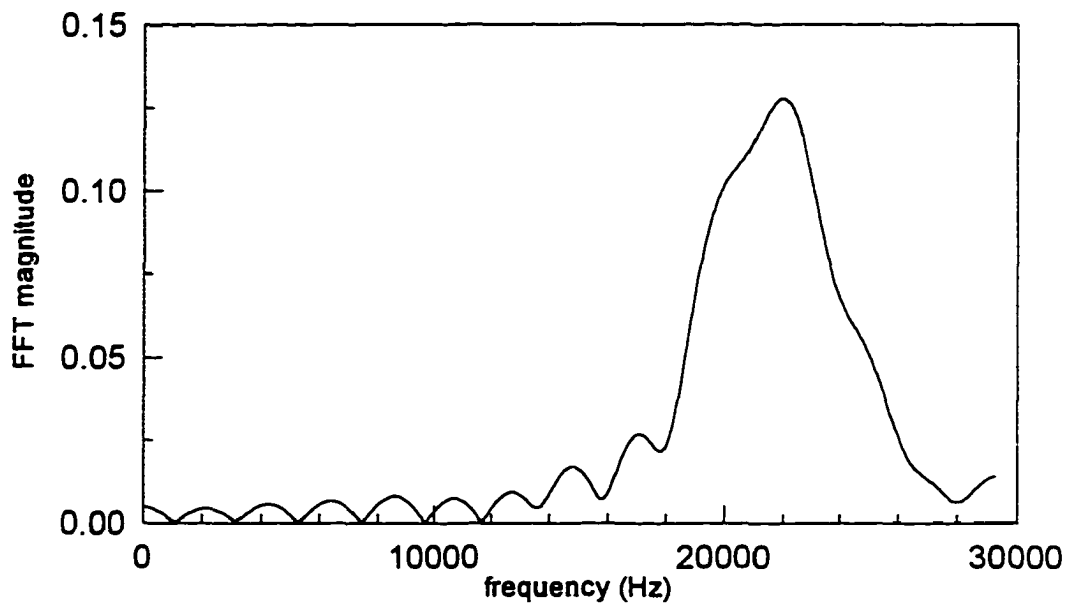
Figure 4.5 A frequency response of an acquired signal where the leakage signal and surface reflection are not resolvable

4.2 Cable Length Compensation

The cables connecting the transmitter and receiver to the altimeter introduce a frequency bias on each received signal. This offset is corrected before the phase of an acquired signal is adjusted for steering delays, otherwise the steering is occurring at the transmitter terminal of the radar source, rather than at the surface of the antenna array.

To measure the 'cable length frequency', a signal is collected while the full length of cable is connected together. (The cables are attached with a barrel connector and 33 dB of attenuators to protect the receiver circuitry.) The cable length frequency is estimated from a frequency response of the signal. The frequency response of a cable length test is provided in Figure 4.6.

After estimating the cable length frequency, its effects are neutralized by shifting each signal's frequency response by the same offset. According to the frequency shifting property

of Fourier transform theory, shifting the spectrum of a sampled signal by a frequency offset, f_{shift}, is equivalent to multiplying each sampled signal by a complex sinusoid

$$X(2\pi[f - f_{shift}]) \Leftrightarrow x(nT_s)e^{-j2\pi f_{shift}nT_s}$$

(4.1)

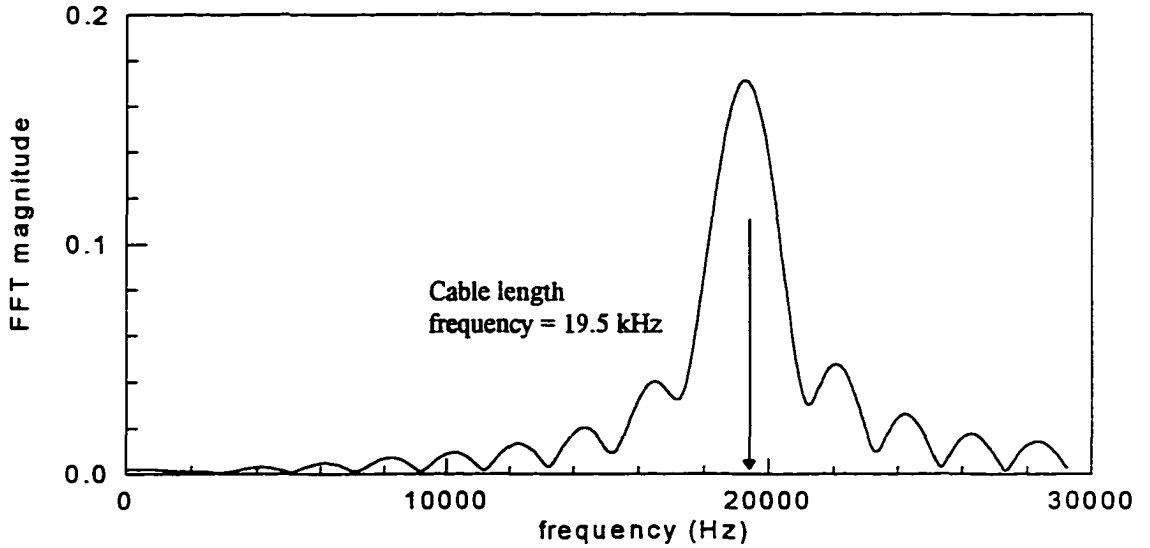where T_s is the sampling period and n is a sample index ranging from 0 to the total number of samples.

Figure 4.6 The frequency response of a cable length test

4.3 Beamforming

The point of the beamsteering algorithm is to steer the antenna array so that it transmits energy toward a patch on the surface, and intercepts the energy reflected by this surface patch. For an FMCW system, the received signals are sinusoidal with frequencies that are equivalent to distances to surface scatterers.

The frequency of a sinusoidal signal can be estimated in either the time or frequency domains using either curve fitting or spectral estimation methods, respectively. In the early stages of the project, several spectral estimation methods were compared for determining the frequency of the dominant sinusoid in the output of the delay and sum beamformer. These included multiple signal classification (MUSIC), autoregressive (AR) modeling, and the fast Fourier transform (FFT). The MUSIC and AR modeling algorithms yielded frequency estimates that were inaccurate, extraneous peaks that could be misinterpreted as returns from

a target, and peak amplitude levels that were not related to the magnitude of the signals. The independent peak amplitudes were typical of high resolution methods representing sinusoidal signals as spikes in the frequency domain. The incorrect frequency estimates and extraneous peaks were, most likely, due to the signals being overridden by noise. Because of its robustness to noise, the FFT was selected for computing the frequency spectrum of signals.

Applying the FFT to a sampled monochromatic signal results in a frequency response having the features of Figure 4.6 (the frequency response of a cable length test). The width of the mainlobe is inversely proportional to the length of the sampling window (in this case, 0.5 ms). If frequency resolution is defined as one-half the null-to-null beamwidth of a sampled sinusoid's frequency response, the frequency resolution of signals sampled for 0.5 ms is 2000 Hz. A narrower beamwidth, corresponding to better frequency resolution, would result from a longer sampling time frame.

For an FMCW system, the window length is bounded by the sweep time. However, unless the bandwidth of the system is increased, improved frequency resolution does not translate to improved range resolution. As an example, consider a FMCW system having a 100 MHz bandwidth and a 1000 Hz modulation frequency (0.5 ms window). With these FMCW characteristics, the 2000 Hz frequency resolution converts to a 5 ft. range resolution. If the modulation frequency is decreased to 100 Hz (changing the frequency resolution of the system to 200 Hz) but bandwidth remains the same, the frequency-to-range conversion reduces to 40 Hz per foot. Although the frequency resolution has decreased, so has the conversion ratio. Consequently, both FMCW systems have a range resolution of 5 ft.

Range resolution defined in the previous paragraph is important when discerning two targets in the field of view of an antenna array. For an imaging system, the ability to resolve peaks (individual scatterers) in the illuminated surface patch is not necessary, because an estimate of the average distance to a patch is all that is desired since, in an image, the patch is represented by a uniform pixel. If it was necessary to resolve two sinusoids in the frequency domain, non-Fourier based spectral estimation methods could be employed; however, these algorithms are more sensitive to noise than the Fourier transform. It may also be possible to decompose the amplitude response of the Fourier transform into a sum of $\sin(x)/x$ functions,

with each function representing the Fourier transform of a windowed sinusoid. By finding a best fit between this model and the Fourier transform of the data, information could be extracted about the frequencies and amplitudes of the sinusoids that were unresolvable in the frequency domain. When tested on noise-free simulated data, this approach yielded accurate results. However, when tested on data from this project, the results were unreasonable; consequently, this does not appear to be a robust approach.

There is some caution in defining the resolution of this system because of the amount of noise present in the current system. If there were no noise present, such that the signals were only from the surface patch being illuminated, the theoretical resolution would be limited only by the spacing between samples in the Fourier transform and the resolution of the altimeter. Defined in this manner, the resolution can be made very fine (by extensively zero-padding the signal), however, the accuracy of the surface estimate could be quite poor if the processed signal consisted mainly of noise.

The outcome of the beamsteering algorithm is a signal dominated by the accumulation of signals reflected by the surface patch. Viewing the frequency response of an output signal from the steering algorithm, estimates of the power reflected by a surface patch and the distance to it are gleaned from the peak magnitude of the response and the frequency where it occurs. The magnitude of the frequency response indicates the strength of the signals reflected by the surface patch. Plotting the squared magnitude as a function of steering direction indicates the power distribution of reflected signals across the surface.

4.4 Spatial Filter

After producing an image of the surface and a power distribution mapping, a spatial filter was applied to the image to smooth areas of low power, which were prone to noise interference. The spatial filter was a weighted, nearest-neighbor averaging algorithm [7]. Each pixel included in the average was assigned a weight based on the power return from that pixel. The value of the weight was the ratio of the pixel's power return to the total power return of all the neighborhood pixels. Thus, pixels with larger power returns, were weighted heavier.

The size of the neighborhood mask was set according to the power return from the pixel being filtered. For most images having 17 × 17 pixels, if the normalized power return from a pixel ranged from 0.25 to 0.50, a 5 × 5 mask was chosen. For pixels with power levels less than 0.25, the mask was expanded to cover a 7 × 7 neighborhood, and if the normalized power return was greater than 0.50, then no filter was applied. The size of the masks and the thresholds were determined experimentally. The goal was to select values which would filter most of the sharp surface changes without removing genuine information about the surface contour. For surfaces with detail, such as small mounds, smaller masks are more appropriate.

All algorithms for data analysis were written as macros for the computer software package MATLAB. The code for the beamforming algorithm is provided in Appendix B.

5 RESULTS AND DISCUSSION

The images in this chapter demonstrate the performance of the surface mapping system for various surface types, surface structures, and noise reduction algorithms. In the chapter, the images are grouped according to surface structure. Besides flat surfaces, the other surface shapes included a surface step change (ridge) on an otherwise flat surface, and a small mound formed on a flat surface.

5.1 Characteristics of the Images

A summary of the figures included in this chapter is catalogued in Table 5.1. Generally, three plots are shown for each surface with two of the plots displaying the image before and after applying a spatial filter, and the third plot showing the power return distribution across the surface. The area along the perimeter of the sand bed is not shown in the surface reconstructions. Because of the weak power return from these areas and the possible interference from signals reflecting off the plywood walls containing the sand bed, the results for these areas are unreliable.

Any surface changes were placed on either the right half or the upper half plane of the surface. The purpose of imaging surfaces with changes in only these two regions was to demonstrate that the imaging algorithm was not preferential towards a specific location or orientation.

The background subtraction method was preferred over the noise estimation and subtraction algorithm for reducing noise. However, for sand surfaces, where the signals reflected by the surface were on the same order of magnitude as the signals reflected by the background data set, the noise estimation and subtraction method was more appropriate. To compare the performance of the background subtraction approach with the noise estimation

Table 5.1 A summary of the figures included in this chapter

Surface	Image	Filtered Image	Power Return From Surface	Method of Noise Reduction		Figure
				Background Subtraction	Estimation & Subtraction	
Level, flat metal plate	✓			✓		5.1
		✓		✓		5.2
			✓	✓		5.3
	✓				✓	5.4
		✓			✓	5.5
			✓		✓	5.6
Flat sand	✓				✓	5.7
		✓			✓	5.8
			✓		✓	5.9
Absorber pads			✓		✓	5.10
Flat sand covered w/ foil pieces			✓	✓		5.11
		✓		✓		5.12
		✓			✓	5.13
Ridge of foamboard	✓			✓		5.14
		✓		✓		5.15
			✓	✓		5.16
Ridge of foamboard	✓			✓		5.17
		✓		✓		5.18
			✓	✓		5.19

Table 5.1 Continued

Surface	Image	Filtered Image	Power Return From Surface	Background Subtraction	Estimation & Subtraction	Figure
				Method of Noise Reduction		
Ridge of sand	✓				✓	5.20
		✓			✓	5.21
			✓		✓	5.22
Ridge of sand w/ foil pieces	✓			✓		5.23, 5.26
		✓		✓		5.24, 5.27
			✓	✓		5.25, 5.28
Ridge of sand w/ foil pieces	✓			✓		5.29
		✓		✓		5.30
			✓	✓		5.31
Mound of sand w/ foil pieces	✓		✓	✓		5.32
		✓		✓		5.33
			✓	✓		5.34
Mound of sand w/ foil pieces	✓			✓		5.35
		✓		✓		5.36
			✓	✓		5.37

34

and subtraction approach, both methods were applied to a couple of surfaces having higher reflectivity than a sand surface.

5.2 Flat Surfaces

Because of its reflective properties and flush nature, the flat metal plate stood as the benchmark test for the imaging system. The reconstructed image of a level, flat metal plate (3 ft. × 3 ft. × ¼ in.) placed on top of the sand surface distanced 7.8 ft. from the antenna array is shown in Figure 5.1. The background subtraction method was applied to reduce noise. (In this case, the images are displayed as both contour and mesh plots. Although mesh plots give a better visualization of the surface, the contour levels in the contour plot provide a better indication of relative surface heights and, therefore, a contour plot is a better tool for evaluating the reconstructed images.)

Although the reconstructed surface appears rugged rather than flat, most of the variation is near the edges. In these regions, the power return is low (Figure 5.3) leading to image degradation caused by noise.

The dominant power return from the center of the surface is indicative of specular reflections, which are expected from a flat surface. When a weighted spatial filter is applied (Figure 5.2), the surface variability is reduced and most of the surface area lies between 7.7 to 7.8 ft from the array. The size of the neighborhood could be increased to level the surface even more, but for surfaces that are not flat, the extended filtering would smooth surface fluctuations. It appears that for this highly reflective surface, the resolution of the imaging system is less than 1.5 in., after filtering.

Because strong signals were received from the metallic surface, it served as a good candidate to evaluate the other interference rejection approach—the noise estimation and subtraction method. Figures 5.4 thru 5.6 are the set of plots exposing these results. Clearly, noise plays a larger influence in areas of low power return than in the image generated when the background subtraction method was applied. The background subtraction method removes the noise more completely and more accurately than the noise estimation and
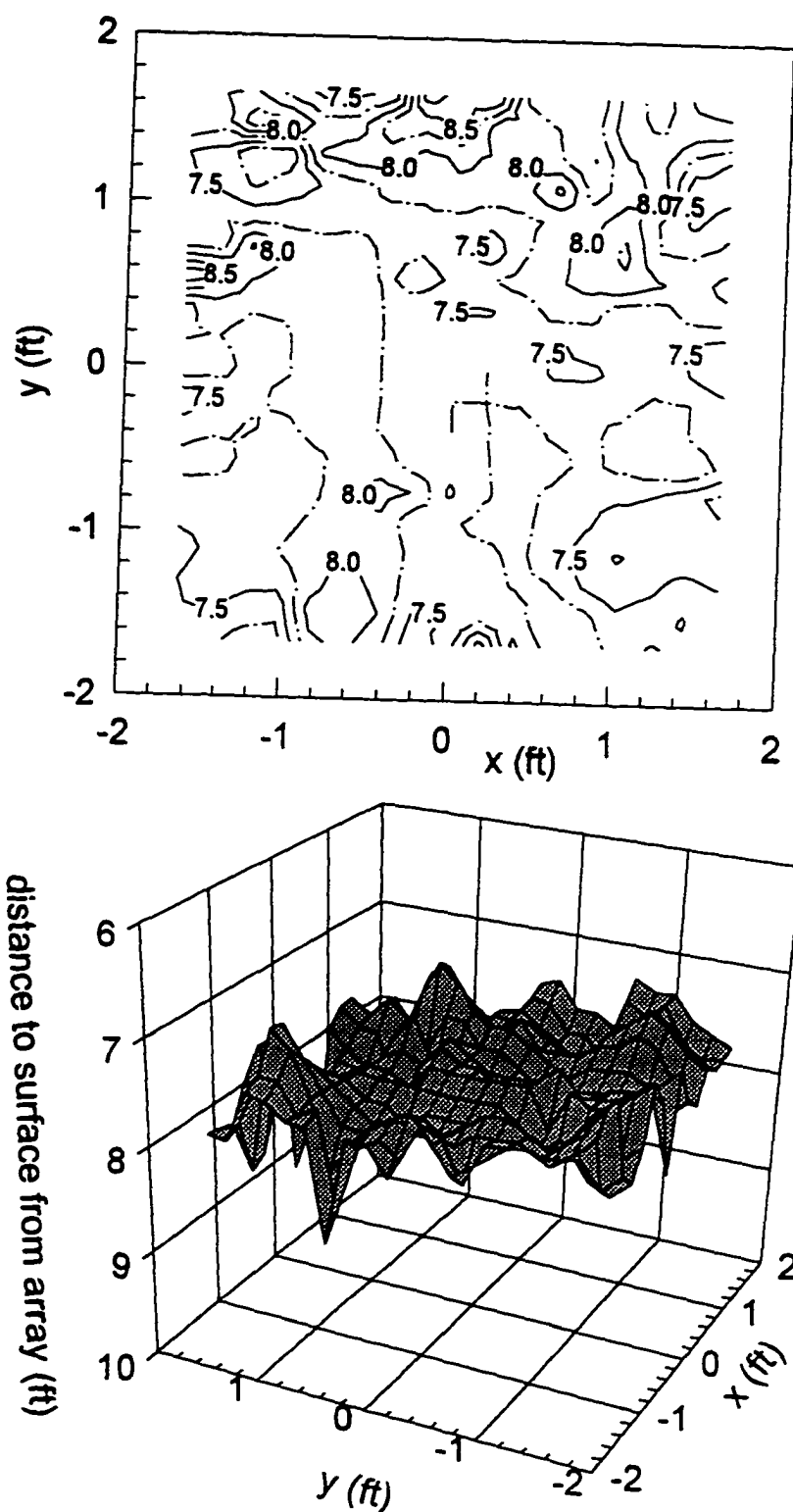
Figure 5.1 Reconstruction of a level, flat metal plate (3 ft × 3 ft) placed 7.8 ft from antenna array. Background subtraction method applied to reduce noise.
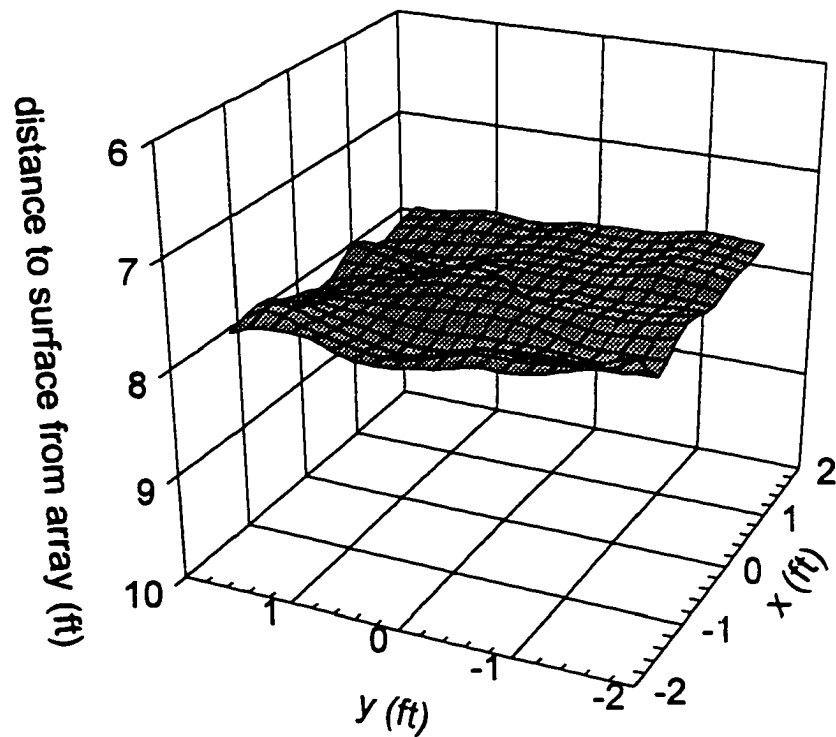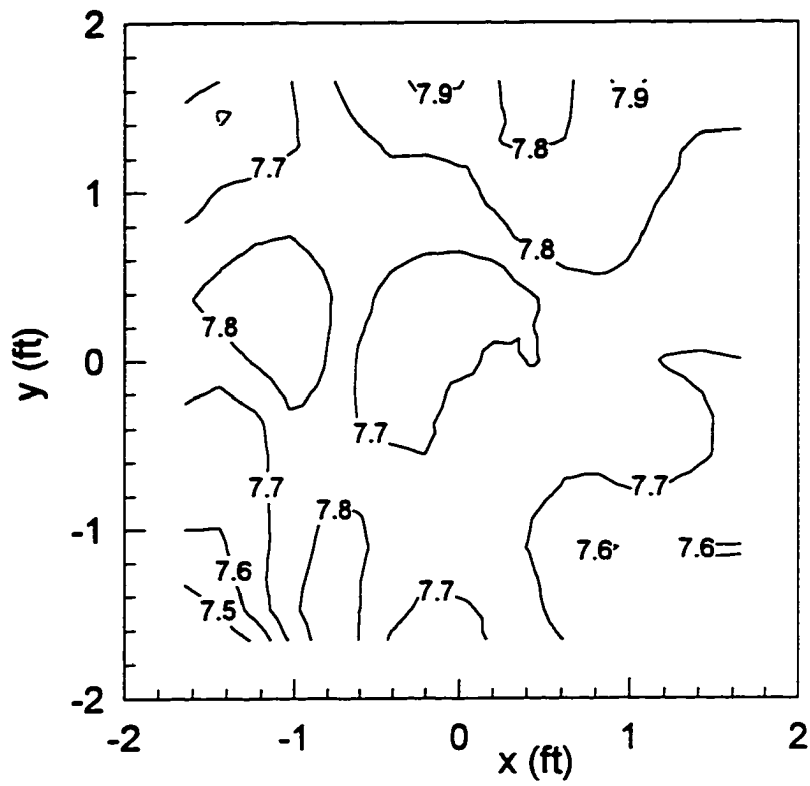
Figure 5.2 The surface of the level, flat metal plate smoothed with a nearest neighbor spatial filter.
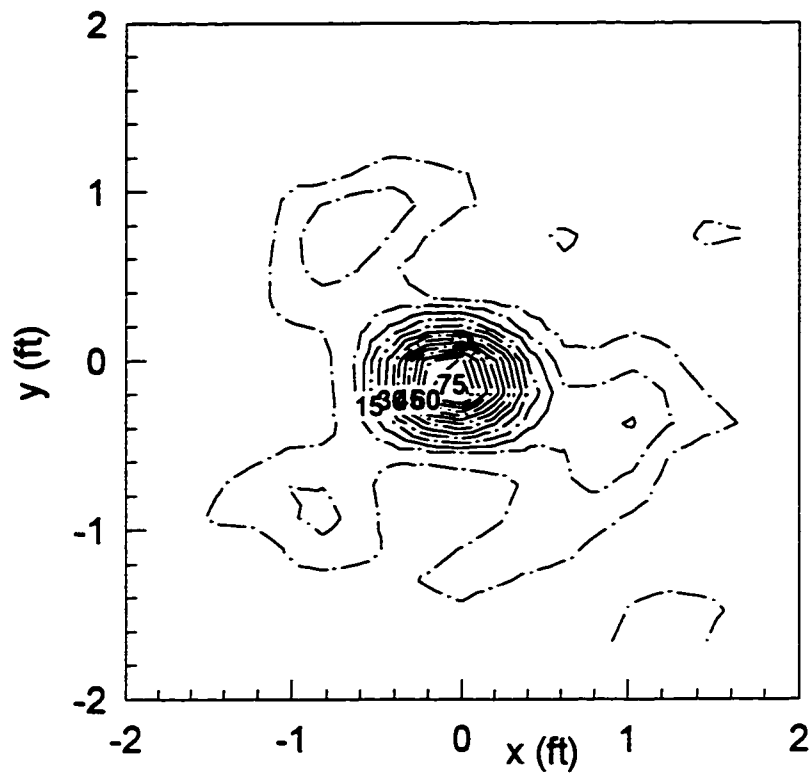
Figure 5.3 Power return across surface of flat metal plate.
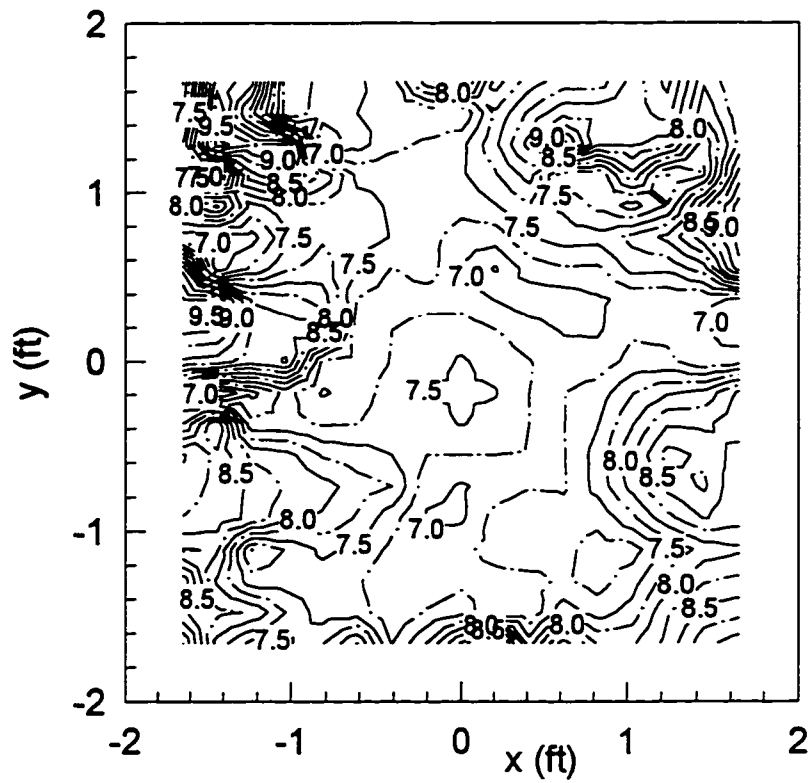

Figure 5.4 Flat metal surface reconstructed using noise estimation and subtraction.
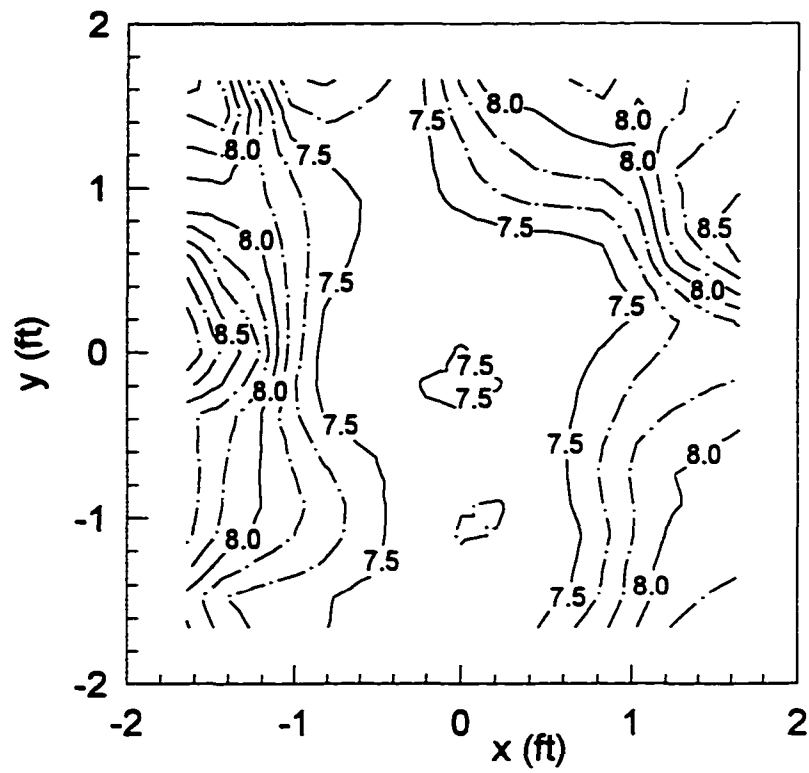
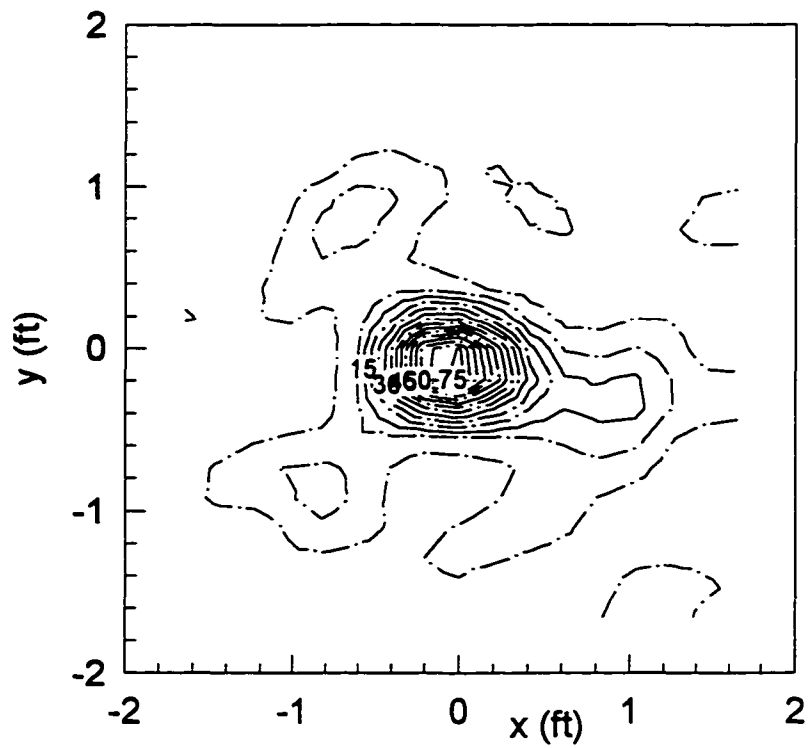Figure 5.5 Reconstructed surface after spatial filtering

Figure 5.6 Power distribution across metal sheet when noise estimation and subtraction algorithm applied.

subtraction method. As a consequence, the background subtraction yields more accurate results; however, as shown in Figure 5.5, the noise estimation and subtraction method does provide a reasonable reconstruction of the surface in areas of strong power return (disregarding a slight bias in the distance estimates).

On the other hand, an image of a flat sand surface estimates surface levels scattered over a 2 ft. range (Figure 5.7). (The noise estimation and subtraction method was used to reduce interference.) The filtered image is plotted in Figure 5.8. Although not apparent from the images, the surface of the sand was located 7.8 ft from the antenna array.

Several factors are affecting the sand surface results. The low power returns (Figure 5.9) imply that noise is likely influencing the surface estimates. In addition, the low power returns indicate that sand is behaving as an absorber. (At 1 GHz, dry sand has an attenuation of approximately 1 dB/m. [19].) The large distance estimates could be caused by signals traveling through the sand bed, reflecting off the plywood sheet below the bed, and returning, in a similar manner, to the antenna array.
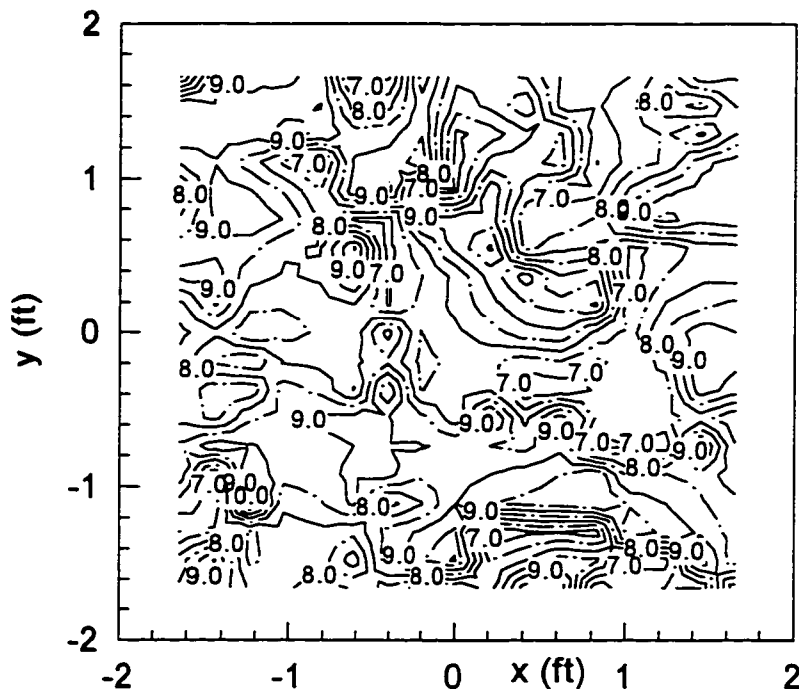

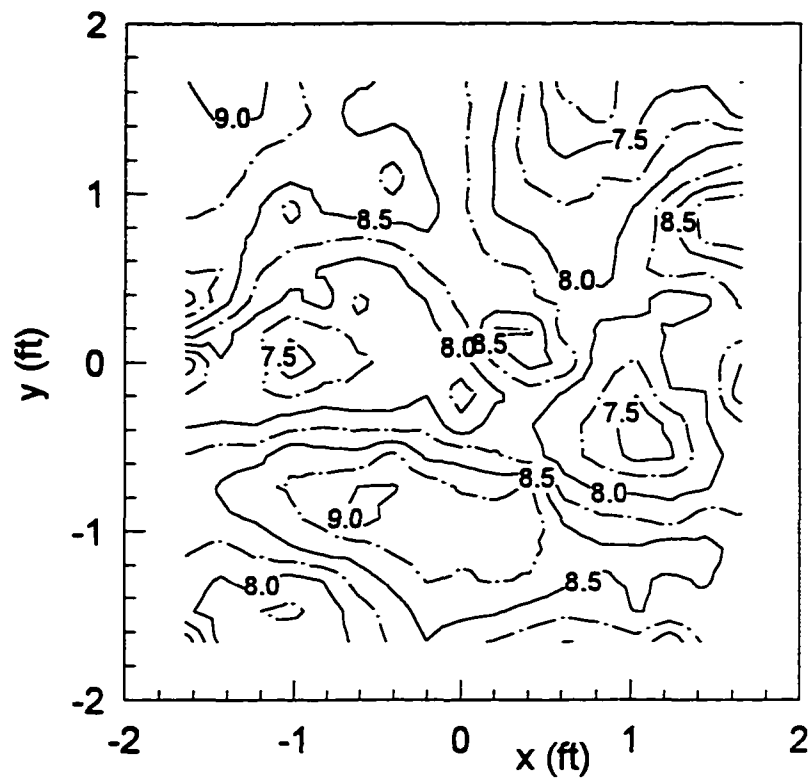Figure 5.7 Image of a flat sand surface before filtering.

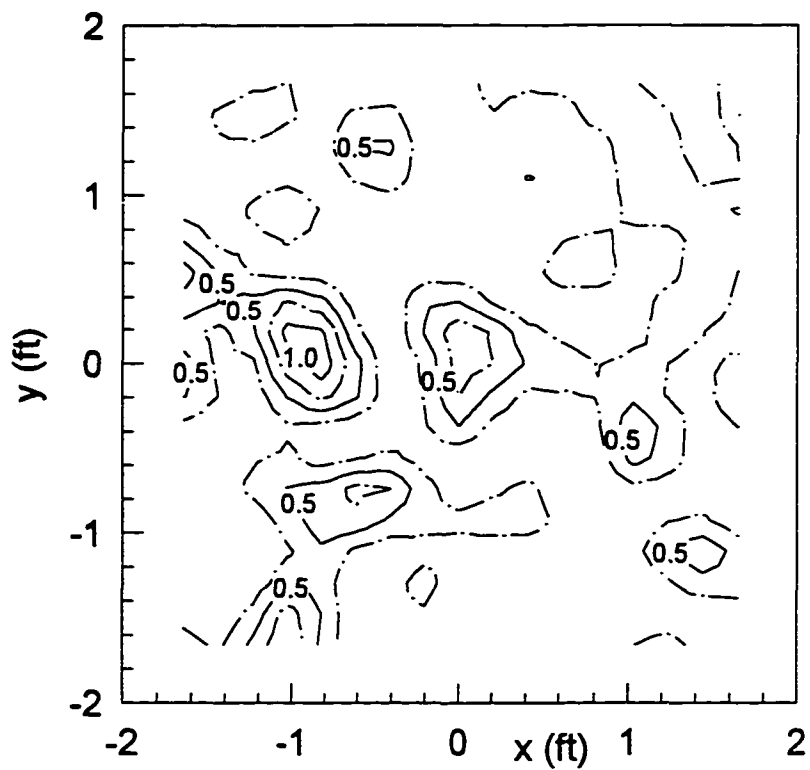Figure 5.8 Image of a flat sand surface after filtering.

Figure 5.9 Power return distribution across flat sand surface.

To demonstrate the similarities between the power return from a surface composed of absorber material with that of sand, Figure 5.10 shows the power return distribution from a surface of five absorber pads, placed side-by-side. (Arranged for acquiring a background data set.) Although distributed differently, the magnitudes of the power returns from the sand surface and the absorber surface are almost equivalent.
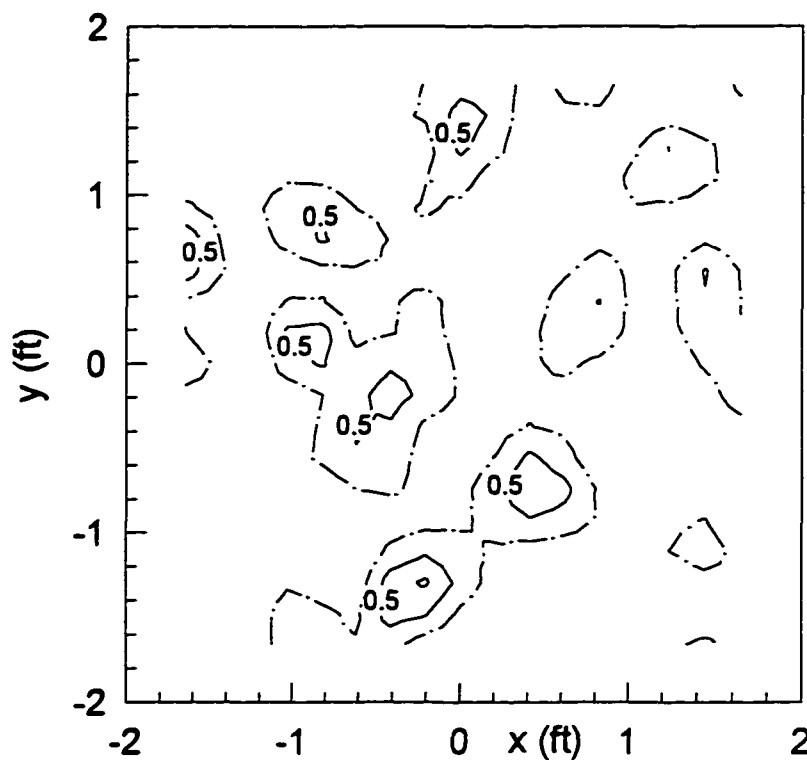

Figure 5.10 Power return distribution across absorber surface.

To improve the reflective properties of the surface, pieces of aluminum foil, ranging in size from 4 in.^{2} to 16 in.^{2}, were randomly dispersed across the surface. Approximately 40% of the sand surface was covered with the small, flat foil pieces. The power return from this surface (Figure 5.11) has a peak value that is more than 10 times larger than the peak power return of the flat sand surface. As a result, regardless of the noise reduction method applied (background subtraction is shown in Figure 5.12 and noise estimation and subtraction in Figure 5.13), the filtered surface contour plots are significant improvements over the flat sand surface reconstructions.
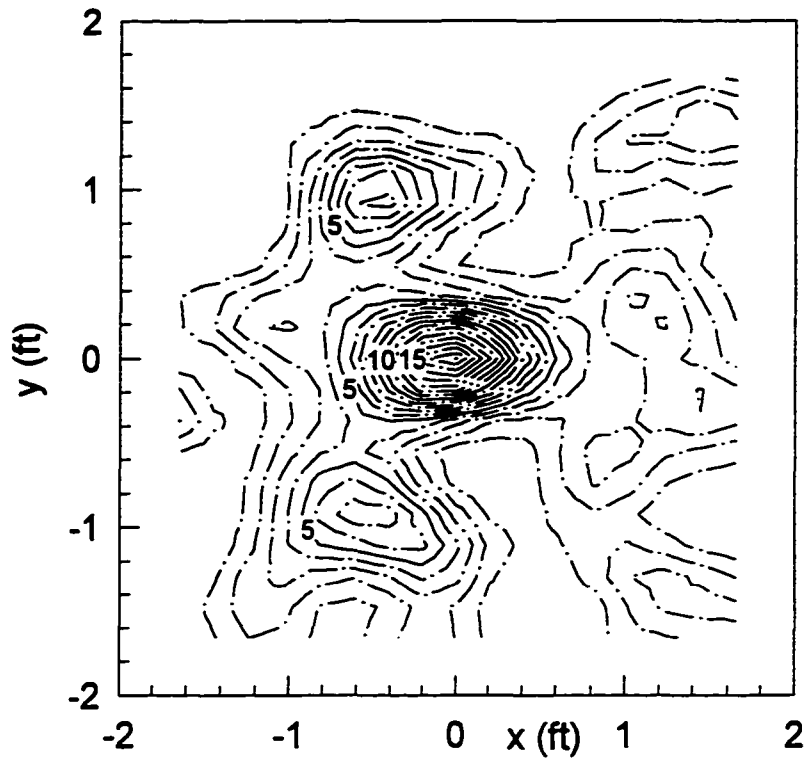
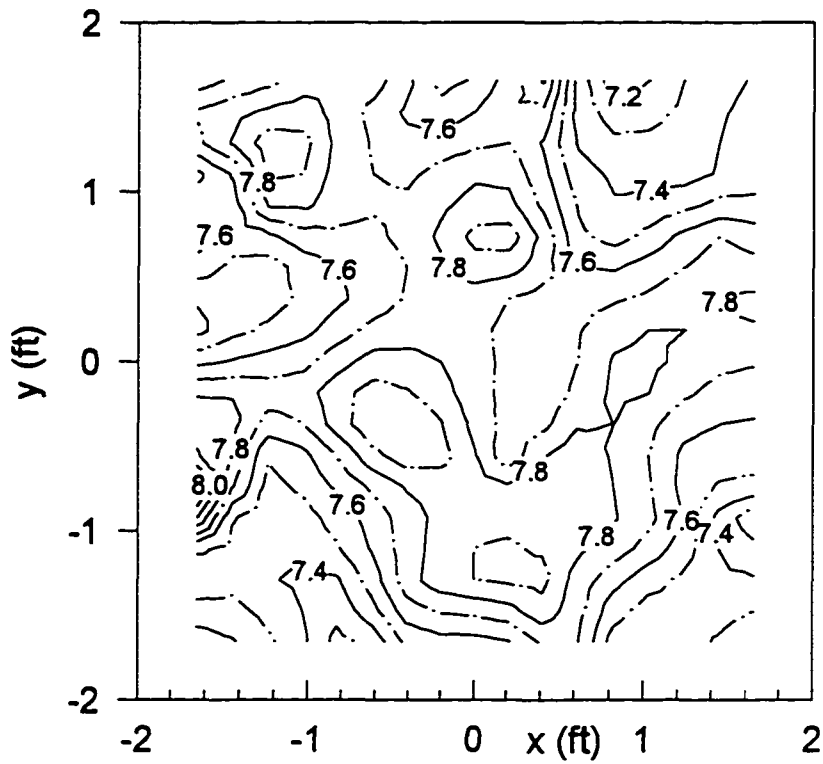Figure 5.11 Power return of flat sand surface partially covered with pieces of foil.

Figure 5.12 The filtered image of the flat surface partially covered with foil pieces.
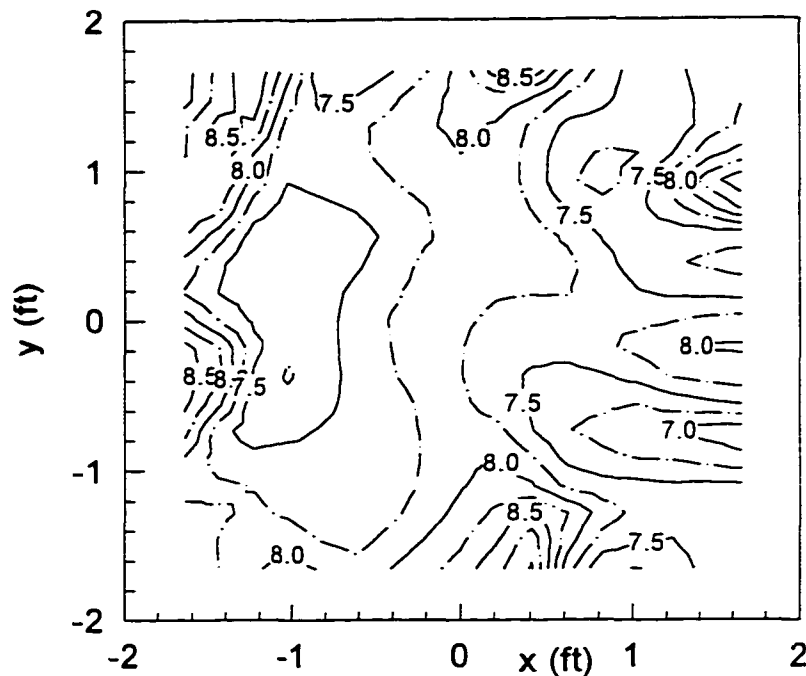(Background subtraction)

Figure 5.13 Filtered image of foil covered surface. (Noise estimation and subtraction)

Even though the power return from the partially foil-covered sand surface is more evenly distributed than the power return from the metal sheet, the peak power return of the foil surface is five times smaller than the peak power return from the metal surface, thus noise has a larger influence on the foil surface results—creating a more variable surface.

5.2 Flat Surfaces with a Ridge

This section includes images of surfaces having a step change placed on an otherwise flat surface. Results from each of the three surface types will be presented.

Since the metal plate could not be bent easily, two sheets of foamboard (each lined with a continuous sheet of aluminum foil) were arranged to create a two-tiered, highly reflective surface. The dimensions of the foamboard sheets were 2 ft. × 3 ft. and 0.5 ft × 3 ft. All of the images of foamboard surfaces applied background subtraction to improve the signal-to-noise ratio.

An image of a two tiered foamboard surface before filtering is shown in Figure 5.14. The image after applying a spatial filter is shown in Figure 5.15. The foamboard strip is
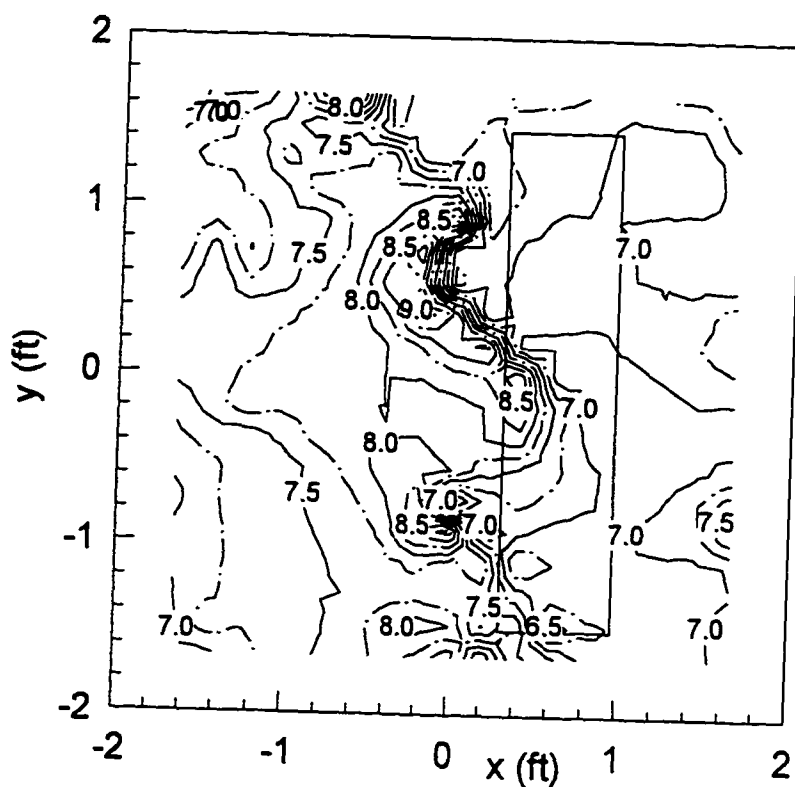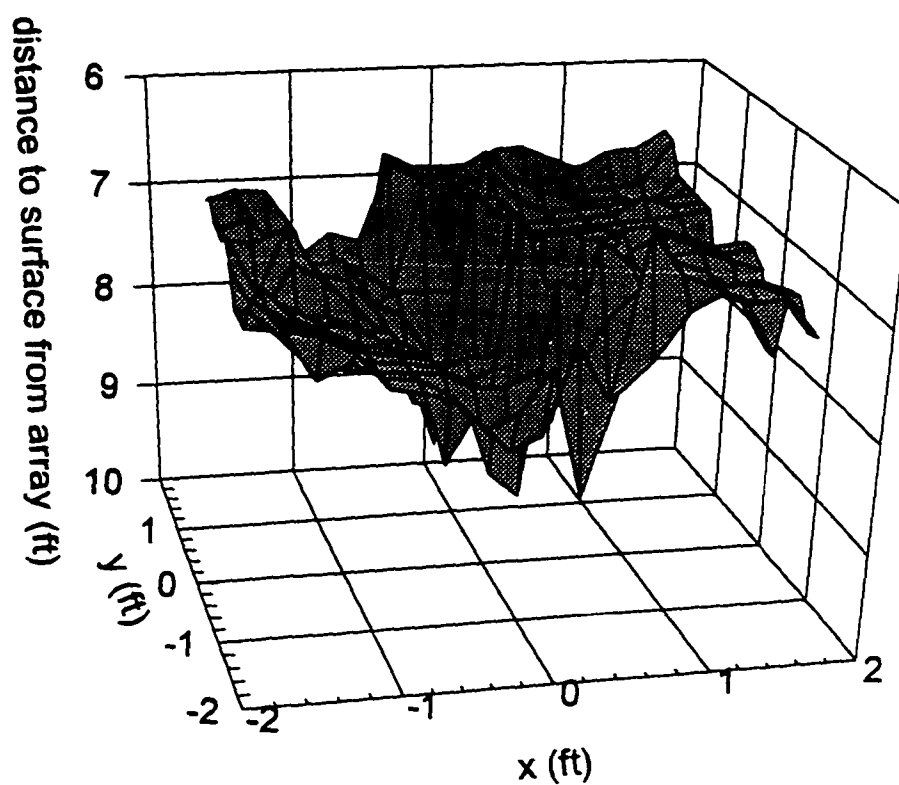
Figure 5.14 Two-levels of foil-lined foamboard. Rectangle indicates location of upper level of foamboard. (Background subtraction)
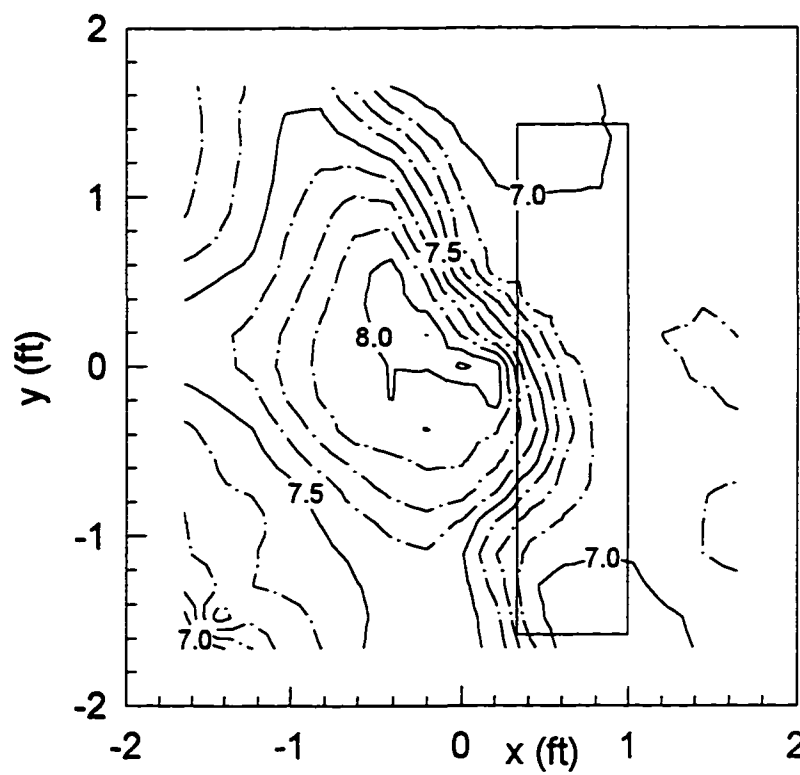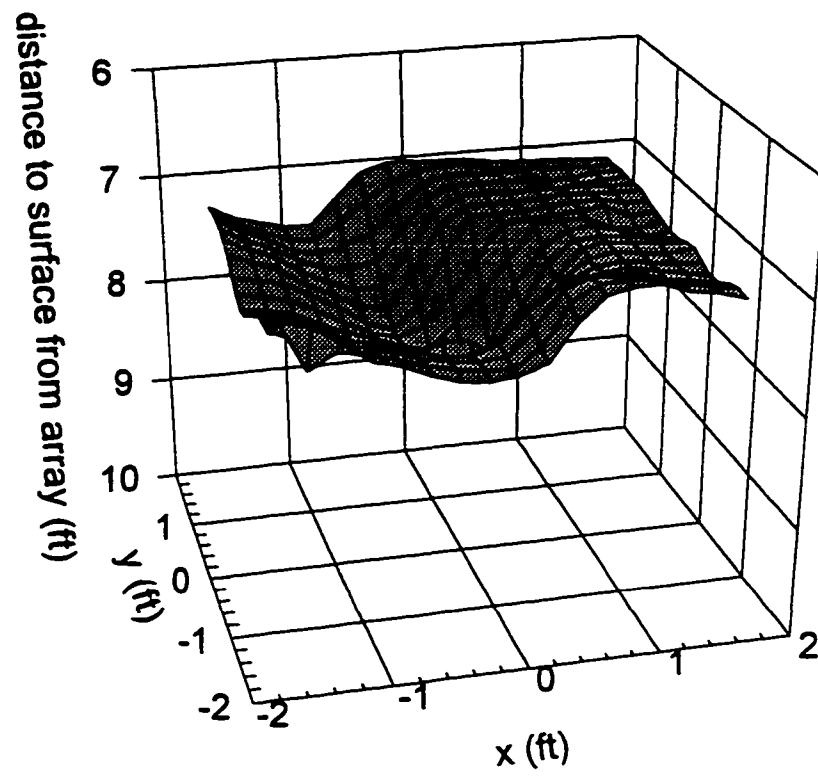
Figure 5.15 Image of foamboard ridge after smoothing. (Box indicates location of ridge.)

placed adjacent to the larger foamboard sheet (located 7.8 ft. from the array), and 0.8 ft. above it. The images that are displayed as contour plots have the location of the foamboard strip outlined in each plot. Clearly, the images reveal the step change in the surface structure. In addition to the images, two regions of strong power return also distinguish the separate specular reflectors (Figure 5.16).
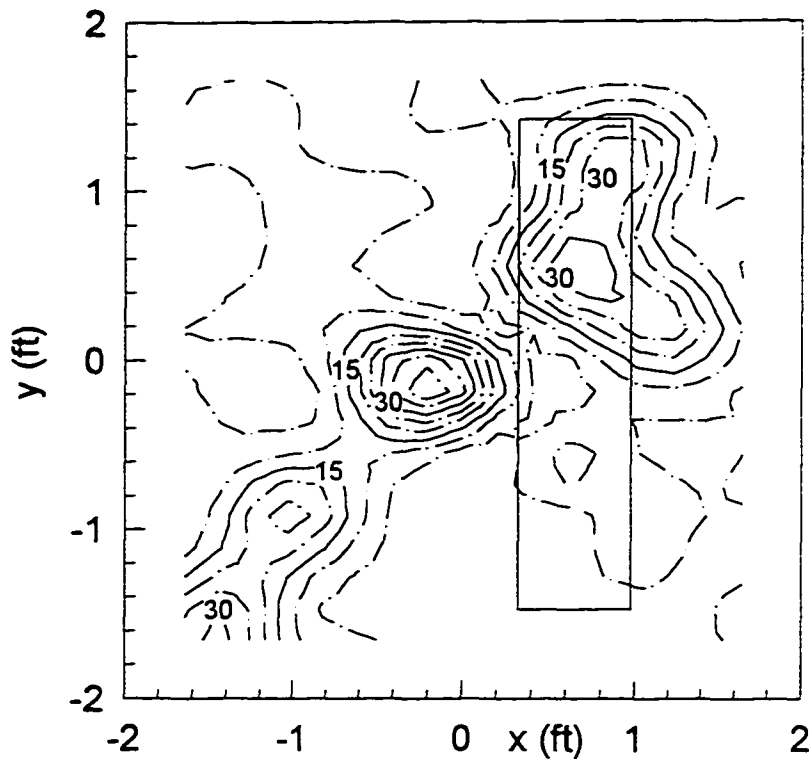
Figure 5.16 Power return across ridged surface. (The location of the ridge is outlined.)

Near the edges of the surface, sidelobe interference may present false surface estimates. The increasing power levels in the lower lefthand corner of Figure 5.16 are from sidelobe interference. The sidelobes of the radiation pattern encircle the main beam at a 2 ft. radius. As the beam is directed toward the corner region, the sidelobes extend over the high-power return area of the ridge, and the beamformer accepts and processes the signals reflected by the ridge as if they were received in the main beam. Furthermore, reviewing Figure 5.14 (the image before applying the spatial filter), the surface estimates in the lower left hand

corner have values similar the ridge.

Similar results are obtained when the previous foamboard arrangement was rotated 90 degrees counterclockwise. The set of plots for this surface structure are presented in Figures 5.17 through 5.19.
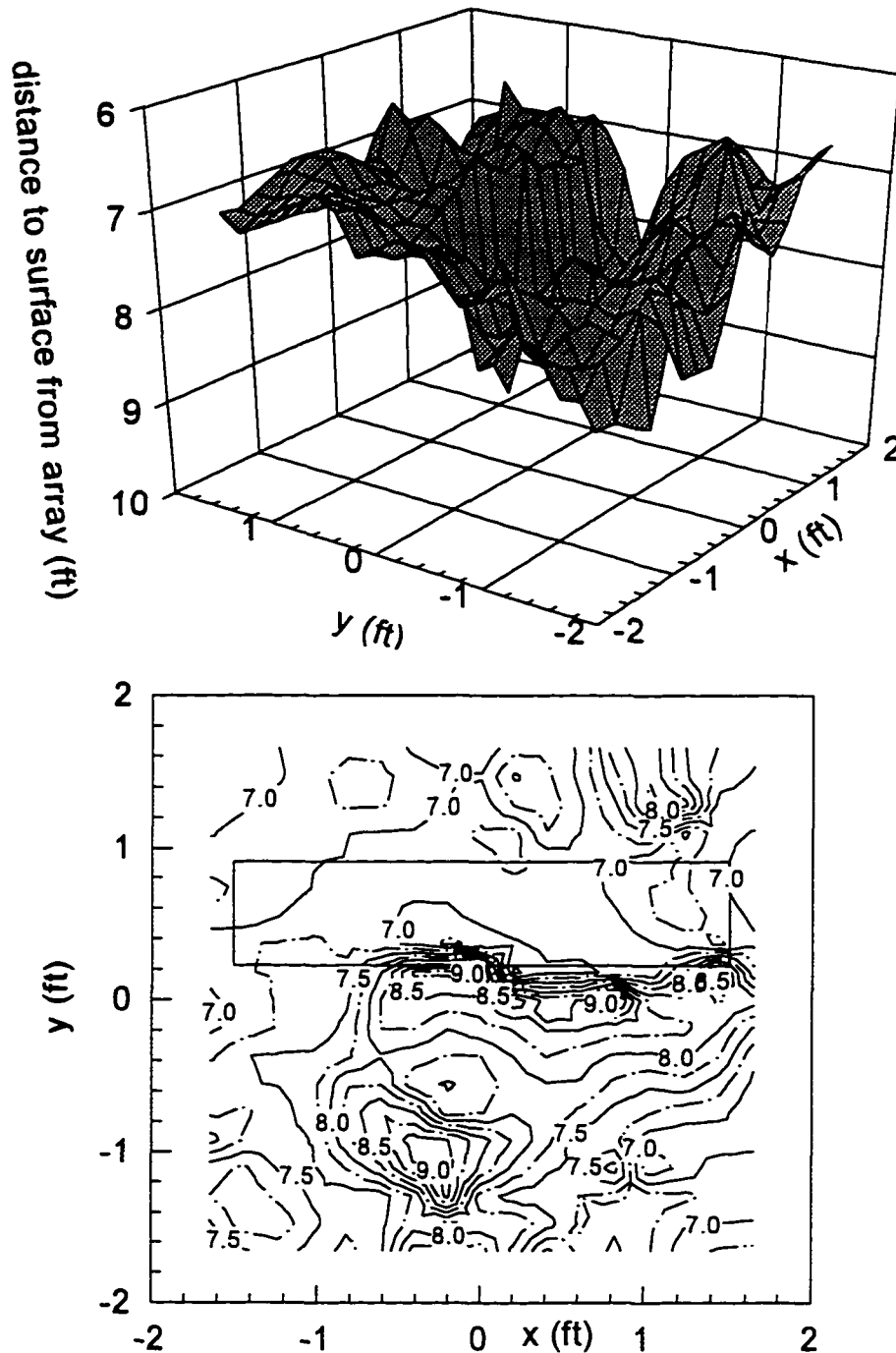
Figure 5.17 Image of foamboard ridge placed parallel to x axis. (Ridge location of outlined.)
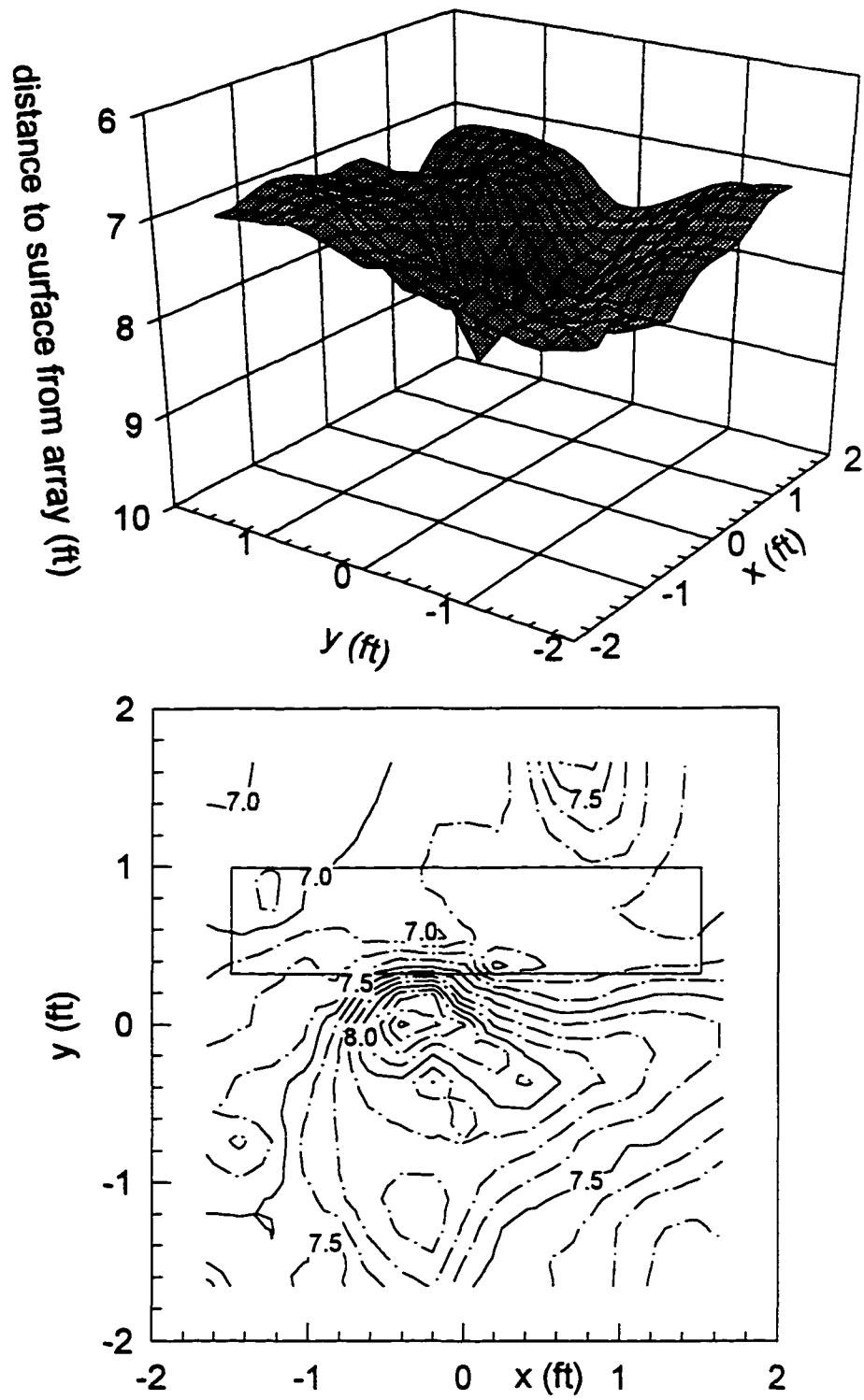
Figure 5.18 Spatially filtered image. (Rectangle indicates location of ridge.)
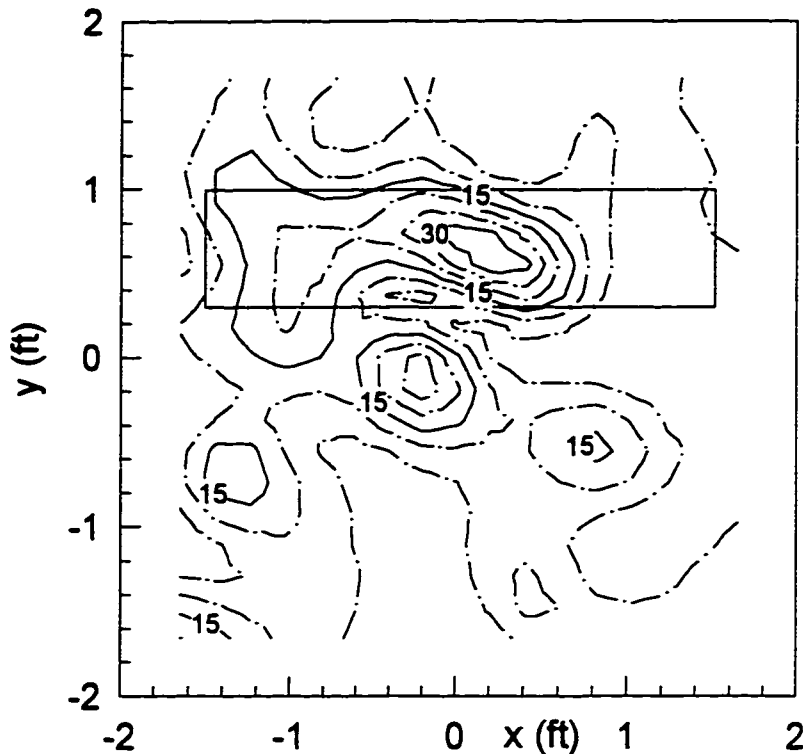
Figure 5.19 Power return distribution across the two-tiered surface.

Note that these images are not 90 degree rotations of the images shown in Figures 5.14 through 5.16. Since the foamboard surfaces were probably not tilted identically among the two surfaces, such that the specular reflections received by the array in each case were different, the power returns across the surfaces are dissimilar. Consequently, noise will influence the images differently and the resulting rotated surface mappings will not be identical.

Viewing the results from the flat metal sheet, and these results of two-tiered continuous foil sheets, it is apparent that the imaging system performs satisfactory when mapping large continuous sections of reflective material.

A 0.7 ft high ridge of sand placed on an otherwise flat surface of sand is reconstructed from the imaging algorithm in Figure 5.20. The noise estimation and subtraction approach was taken to reduce interference. With the extreme surface changes, it is infeasible to discern anything about the surface from the unfiltered image. The numerous drastic surface changes are misleading, but not unexpected since the power return across most of the surface (Figure

5.21) is weak. After applying a spatial filter, the image (Figure 5.22) indicates a portion of the ridge. However, this result may be a coincidental response to noise since the power return in this region is weak. With the small power return across much of the surface, the results are unreliable and inconclusive.
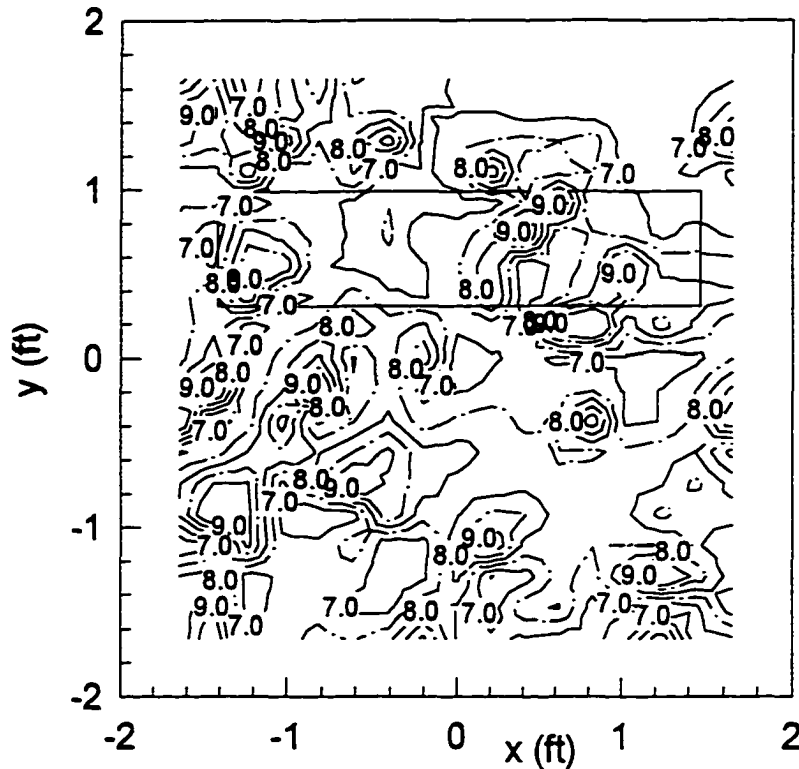
Figure 5.20 Image of a 0.7 ft high ridge of sand. (Location of ridge is outlined.)

For the next set of figures, a 0.6 ft. high ridge was sculpted on top of a flat sand surface and covered with randomly dispersed flat foil pieces. Images of the surface, before and after filtering, are shown in Figures 5.23 and 5.24. Although the ridge is not as well defined as it was for the equivalent foamboard surface, the shape of the reconstructed surface indicates a surface change in the general region of the ridge. The power return distribution across the surface is shown in Figure 5.25.
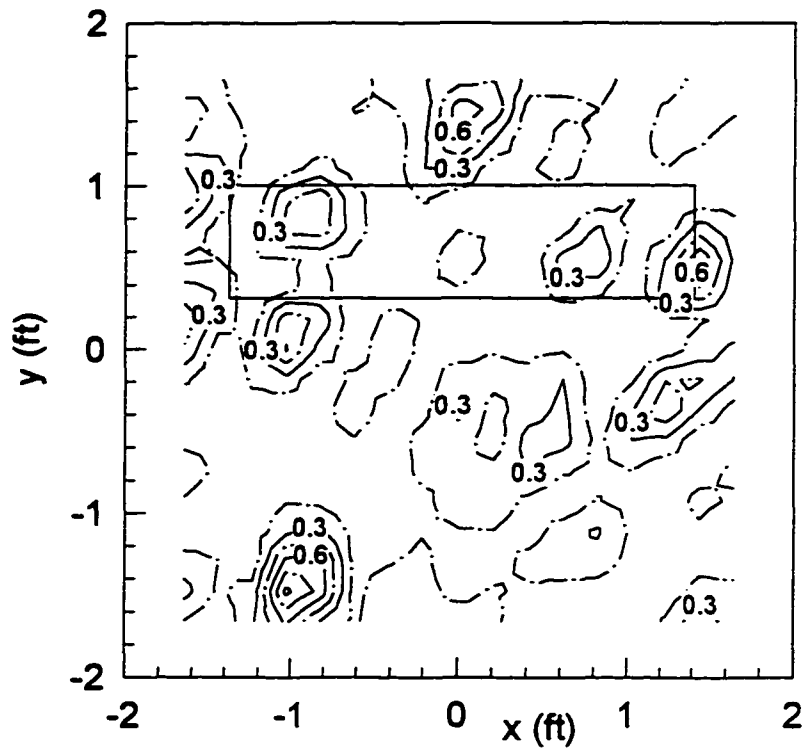
Figure 5.21 Power return distribution across sand surface having a ridge.
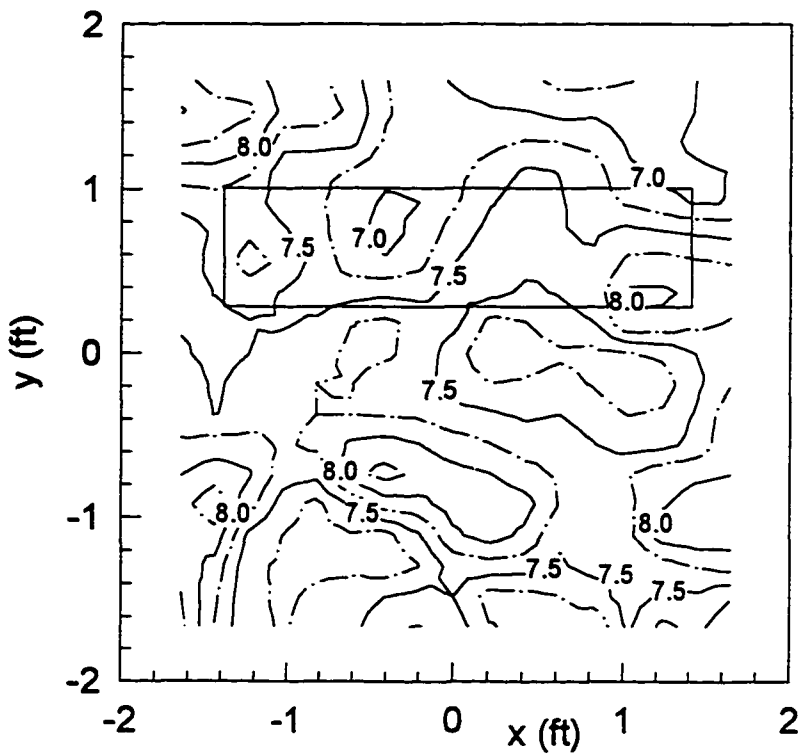
Figure 5.22 Smoothed image of a sand surface having a 0.7 ft. ridge located in the area outlined.

The next three plots (Figures 5.26 through 5.28) are of the same sand surface, but the foil pieces had been removed and redistributed in a random fashion. Comparing this set of plots with the previous set, it is apparent that the images and the power returns from the surface depend on the arrangement of the foil pieces. This is most noticeable when viewing the power returns across the surfaces.
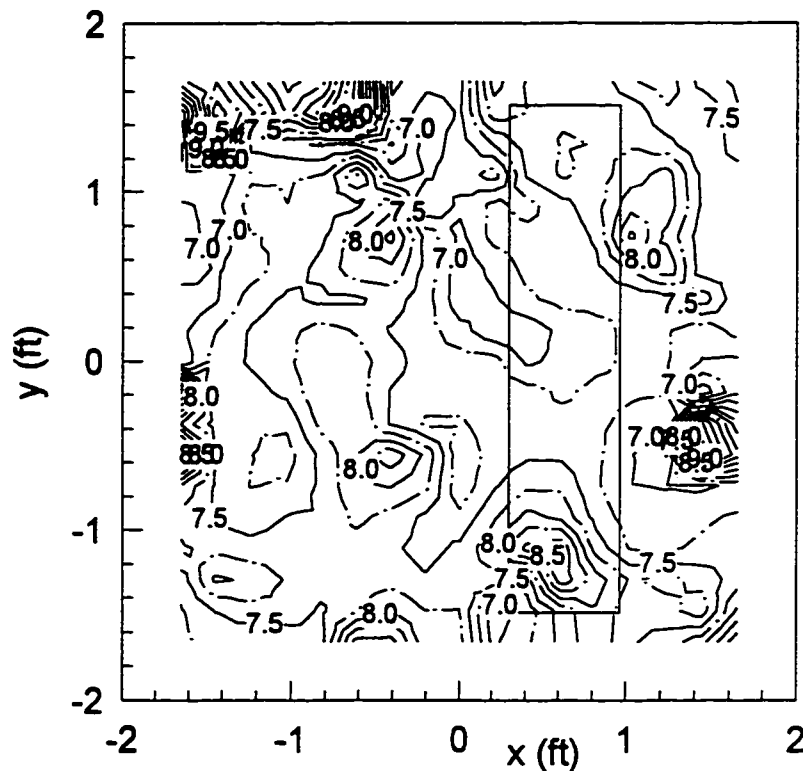
Figure 5.23 Image of a sand surface covered with foil pieces having a 0.6 ft high ridge.

Since the foil pieces are dominated by specular reflections, the power return across the surface will depend on the orientation of the flat foil pieces. Viewing Figure 5.28, the largest power return is near the edge of the surface, rather than the center, as it was with the continuous metal sheets. It is likely that a piece of foil near the edge was tilted more favorably toward the antenna array so that more of its specular reflections were received.
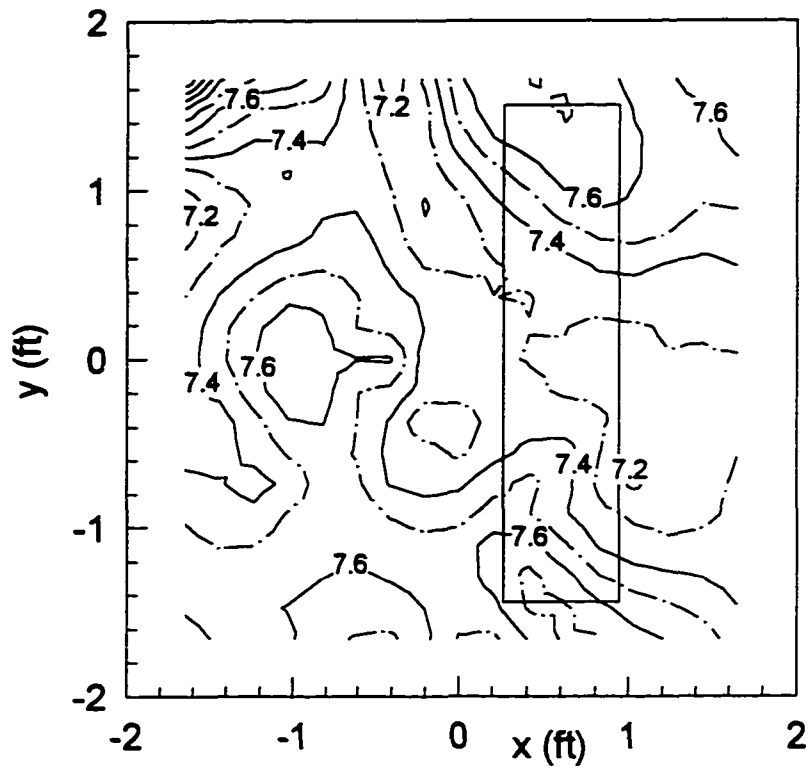
Figure 5.24 Filtered image of foil dotted sand surface having a ridge.
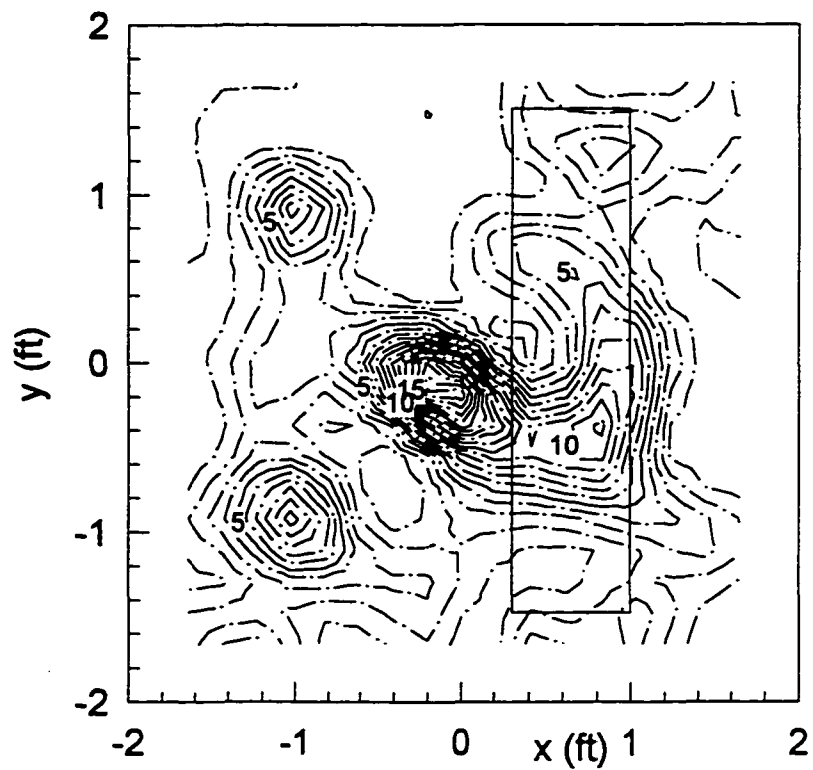
Figure 5.25 Power return across ridged sand surface covered with foil pieces.
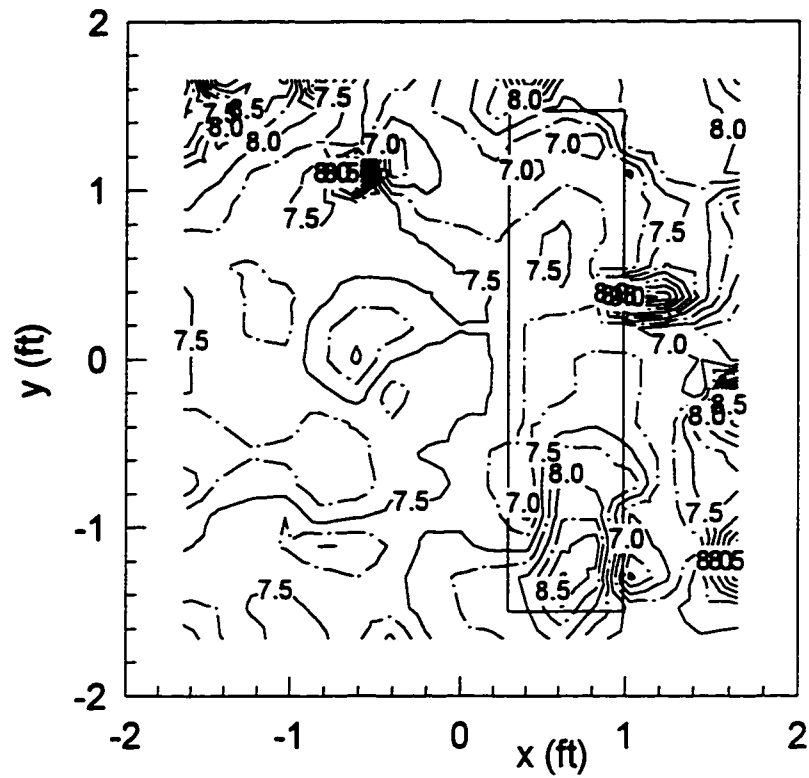
Figure 5.26 Image of a sand surface covered with foil pieces having a 0.6 ft high ridge.
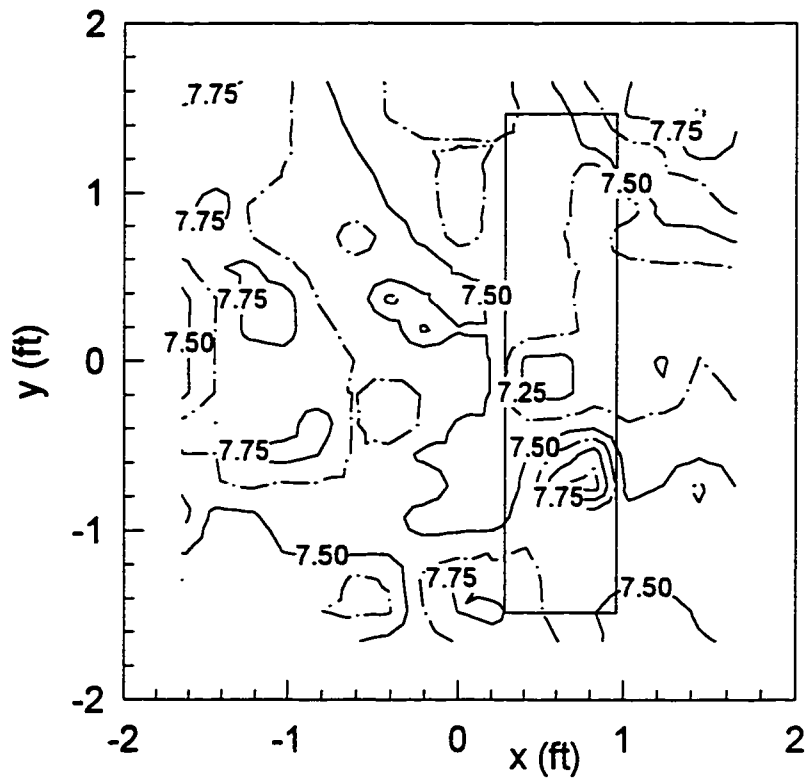
Figure 5.27 Filtered image of ridged surface partially covered with foil pieces.
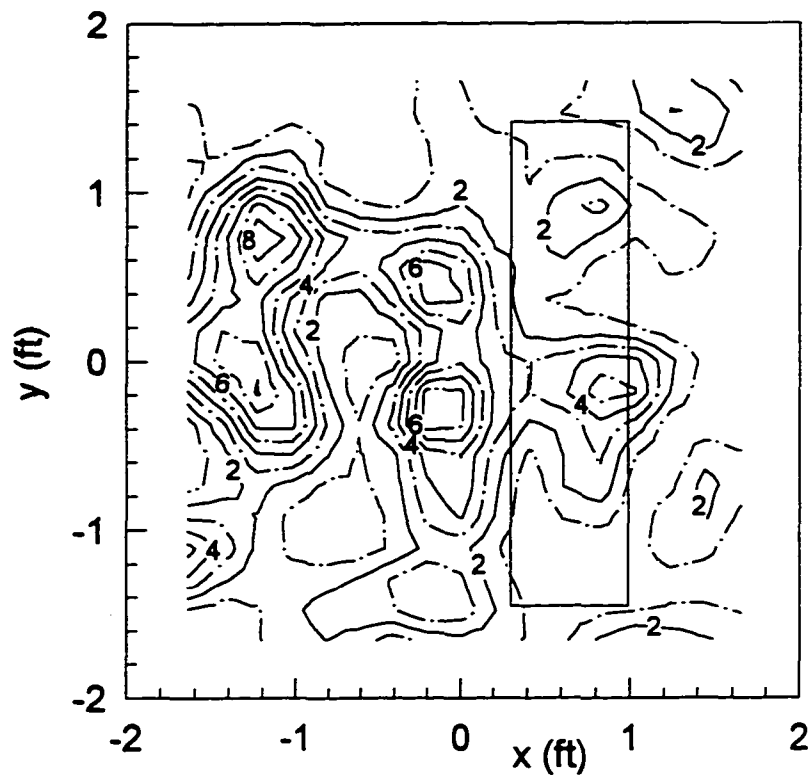
Figure 5.28 Power return across surface covered with foil pieces.

If many of the foil pieces are tilted away from the antenna array, the power return across the surface will be small and noise could have a large influence on the reconstructed images. For this reason, it would be advantageous to image a surface that is not dominated by specular reflections. A surface that is rough, yet reflective, such that the power return is evenly distributed across the surface, yet strong enough to overcome the large noise sources present in the system, would produce accurate images more consistently.

The image of a 0.6 ft. high sand ridge placed parallel to the x axis with foil pieces partially covering the entire surface of the sand bed is shown in Figure 5.29. The location of the ridge is enclosed in the rectangle. It appears that part of the surface enclosed in the rectangle displays an upward trend, indicating the ridge. However, when the image is filtered (Figure 5.30), the height of the ridge is reduced and the trend is not as obvious. Viewing the power return distribution across the surface (Figure 5.31), the regions in the rectangle where the trend occured are areas of low power return. As a consequence, this surface trend was smoothed out when the spatial filter was applied.

The small peak in the power return distribution located at (0, 1 ft.) could have been caused by a sidelobe in the radiation pattern receiving signals from the area near (-1 ft., -1 ft.). This would explain the similar surface levels of these two areas shown in the filtered image. Because of the low power return from other areas within the rectangle, this surface level dominates the region and in effect, flattens the ridge when the spatial filter is applied.
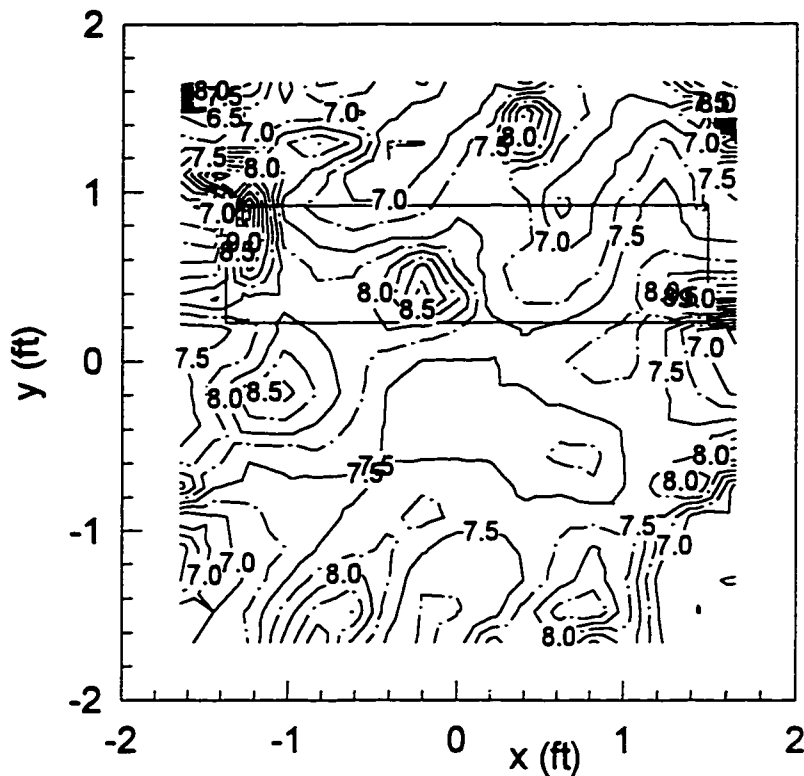
Figure 5.29 Image of a 0.6 ft high ridge of sand. Sand surface covered with foil pieces.

5.4 Flat Surfaces with a Mound

To test the resolution of the imaging system, a small mound of sand (approximately 1 ft. long × 0.5 ft. wide × 0.5 high) was piled on the flat sand surface. The entire sand surface, including the flat section and the mound, was partially covered with the flat foil pieces.
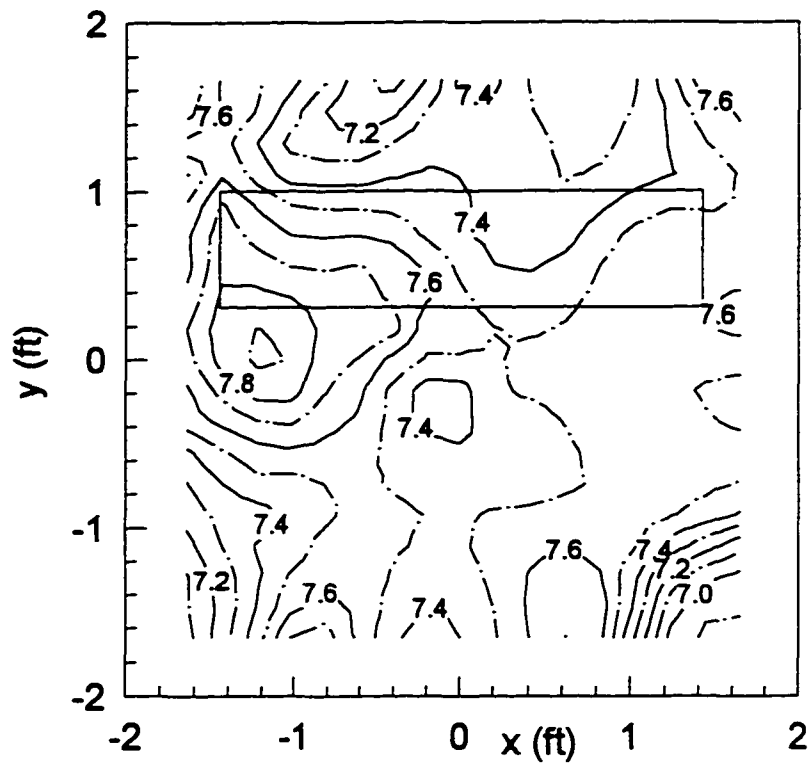
Figure 5.30 Filtered image of foil surface with ridge.
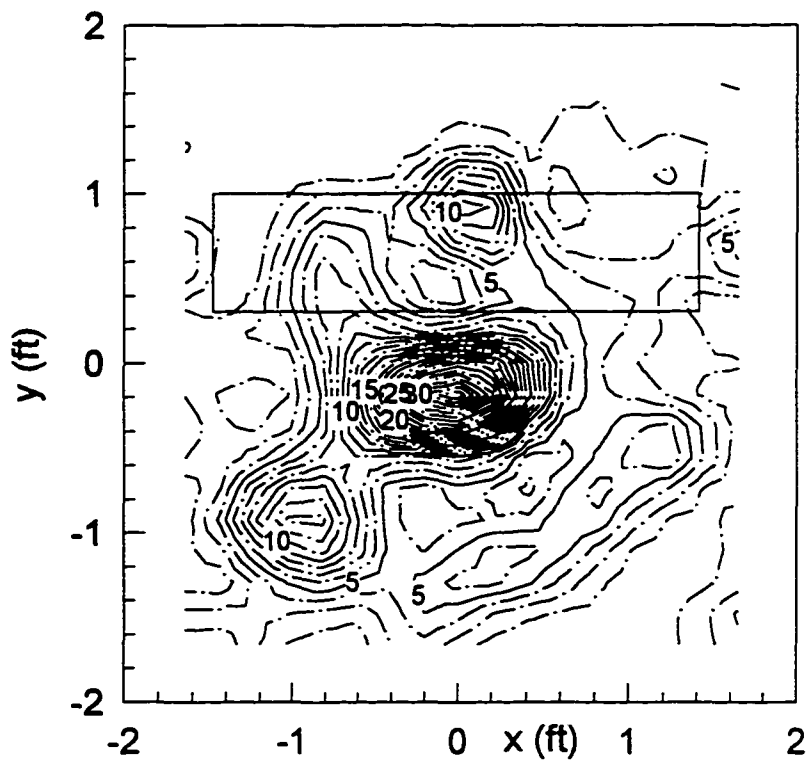
Figure 5.31 Power of signals reflected by surface.

A set of plots for one placement of the mound are shown in Figures 5.32 thru 5.34. Although the mound is not apparent in the unfiltered image of the surface, there is definitely a surface change in the filtered image at the region where the mound was located. In addition, the power return distribution indicates a small peak at the location of the mound.

An image of the mound positioned at a different location is shown in Figure 5.35 and the filtered image for this surface is plotted in Figure 5.36. The unfiltered image indicates a 6 in. surface change in the area of the mound, however, because of the strong power return from this region (Figure 5.37), the presence of the mound at this location is more apparent in the filtered image.

These last sets of images indicate that this radar system is capable of resolving a 6 in. high mound on a flat surface. This resolution is attainable under the condition that the power return from the mound is strong enough so that the mound is not smoothed out by adjacent areas when the spatial filter is applied. In addition, for best results, there should be fairly even power return distribution across the remaining surface so that interference from noise does not affect the accuracy of the image.
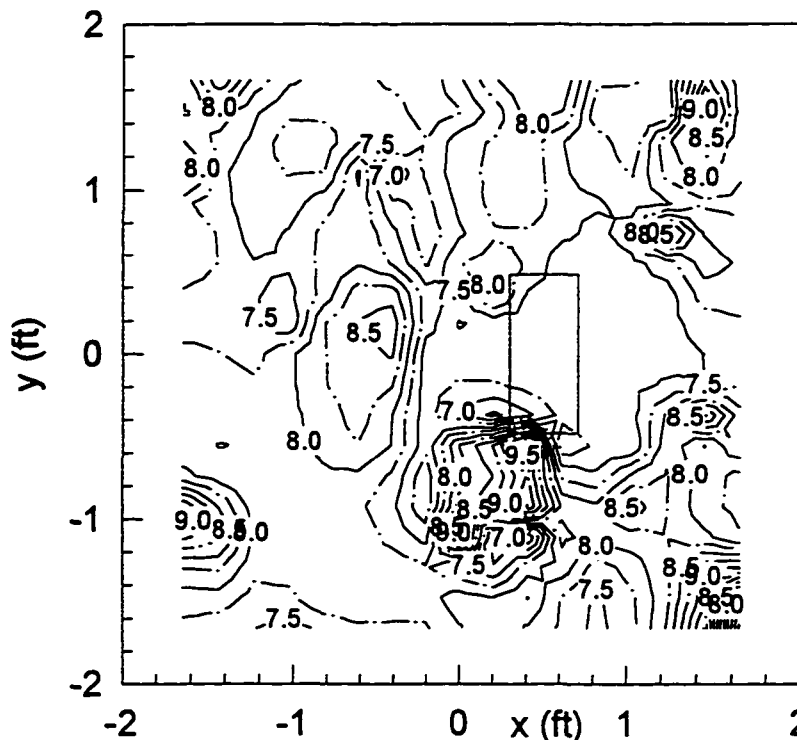
Figure 5.32 Image of a sand mound, 0.5 ft high, with surface covered with foil pieces.
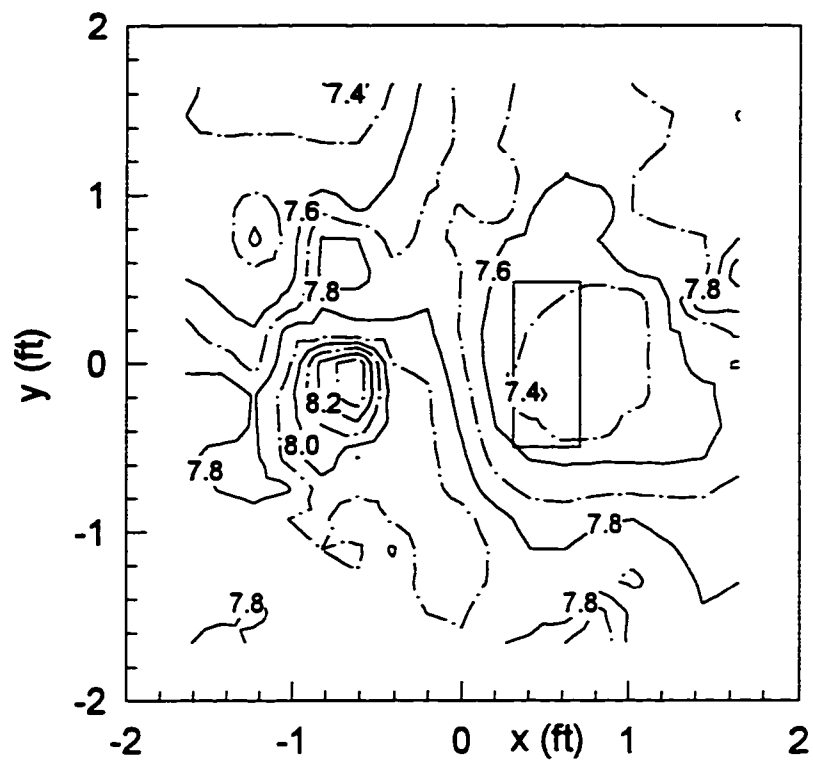
Figure 5.33 Filtered image of the surface having a mound.
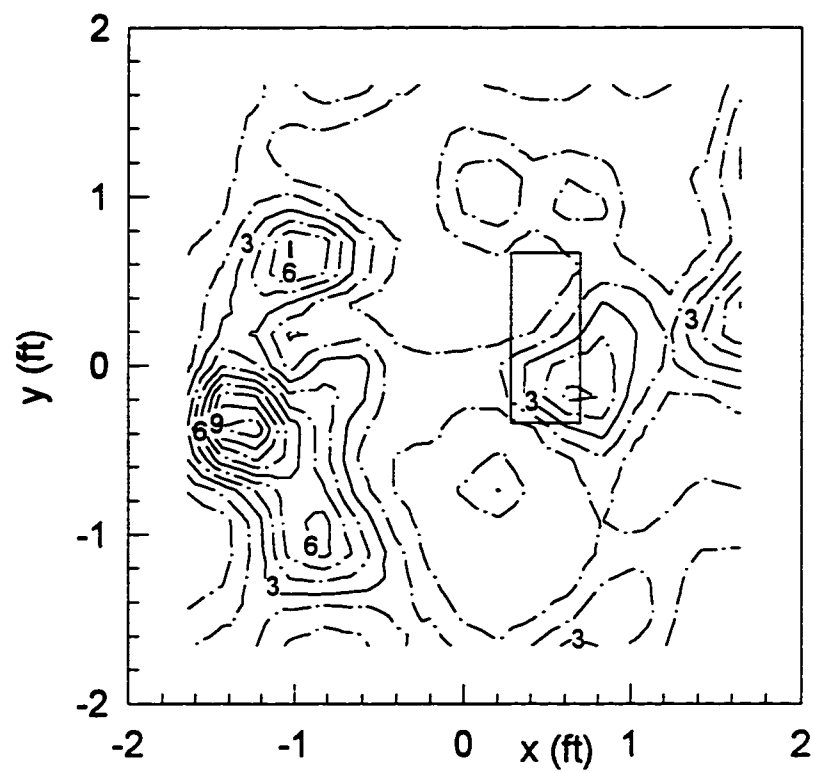
Figure 5.34 Power return from surface with mound.
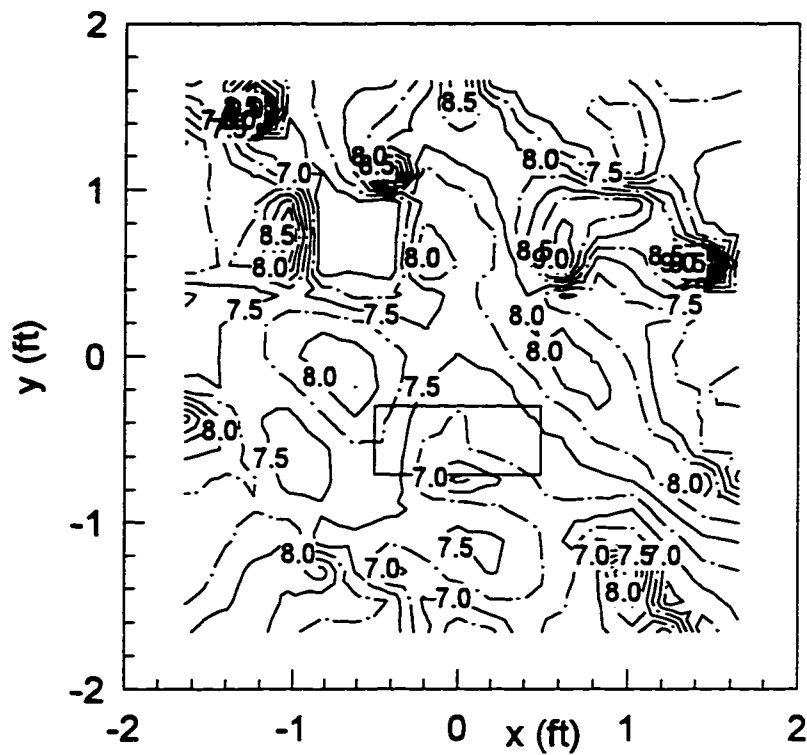
Figure 5.35 Image of a 0.5 ft high mound of sand covered with foil pieces. (The rectangle indicates the location of the mound.)
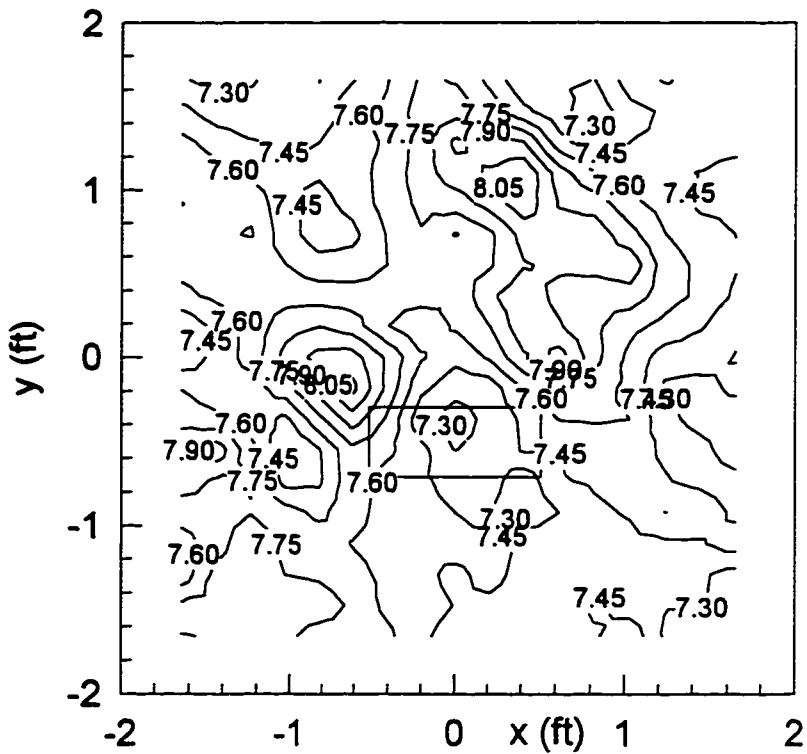
Figure 5.36 Filtered image of foil covered sand surface with mound.
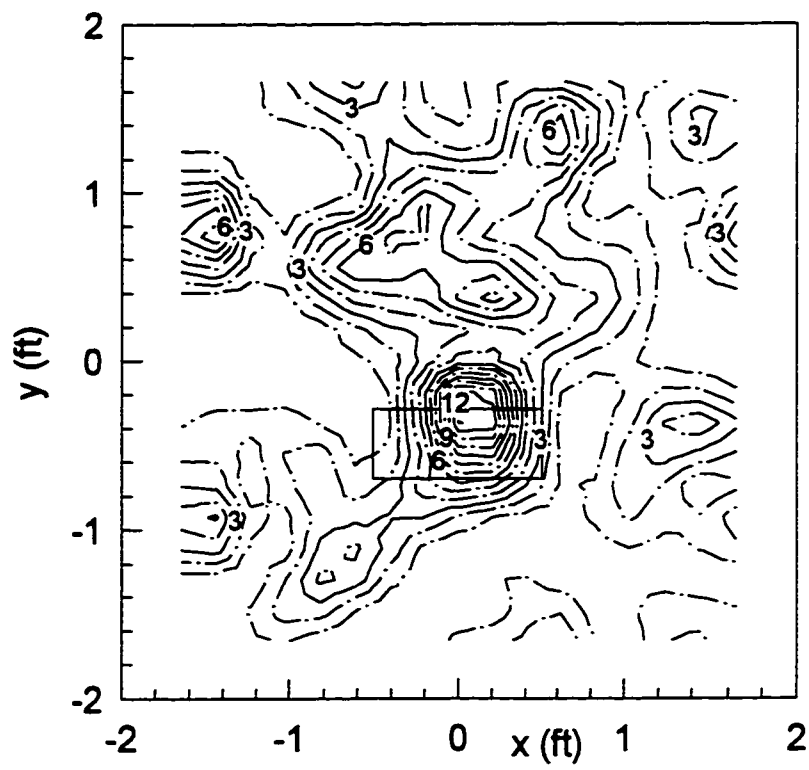
Figure 5.37 Power return across sand surface partially covered with foil pieces having a 0.5 ft high mound.

6 CONCLUSIONS

Surface characteristics of a fluidized bed combustor contain information about the dynamic behavior of the combustion bed. A real-time surface mapping would be a beneficial tool for diagnosing problems occuring within the bed, such as agglomeration, before the performance of the combustor unit is severely degraded.

The purpose of this project was to develop a proof-of-concept phased array surface contour mapping system. The system was designed to image the surface of a cold static bed, and could later be hardened to withstand the harsh conditions within a reactor.

The surface mapping system demonstrated limited success. Despite efforts to reduce noise, especially cross talk among elements, the small scattered fields from homogeneous sand surfaces created difficulties for the radar system in producing contour maps of this type of surface. On the positive side, for surfaces with higher reflective properties, simple surface changes were detectable, and in areas of strong power return, the estimated elevation changes were reasonably accurate. Indeed, when imaging a flat metal plate, the variation across the reconstructed surface was within ± 1.5 in. Therefore, the major problems of this system were not with the beamforming algorithm or the procedure for estimating surface range, but rather limitations caused by scattering characteristics of the surface material and interference from leakage signals and other noise sources.

With this in mind, there are several modifications to the system hardware that should be addressed in future work. One of the improvements should be a redesigned antenna array. Besides beamwidth considerations and geometric arrangement, the design must strive to eliminate cross-talk among elements. Although signal processing tools are available to reduce noise, these methods have imperfections and, as a result, introduce phase distortion and other noise. In designing a new array, consideration should be given to enlarging the array to permit the use of horn attachments. Furthermore, if a circular array is necessary because of

system constraints, the elements should be placed in concentric rings so that amplitude weighting could be incorporated into the beamsteering algorithm to reduce sidelobe interference.

This system demonstrated that the reflective nature of the surface played an important role in the performance of the system. Although the composition of the fluidized bed was assumed to be homogeneous sand, the presence of foreign particles, such as metal shards, within a bed, or a bed composed of a more reflective substance, is conceivable. Whereas flat foil pieces were placed on the sand surface, a test bed consisting of metal shot dispersed among glass beads would have better scattering properties than the pure sand surface, yet reflections would not be as specular as the foil, and, in addition, the power return across the surface would be more evenly distributed.

Along these lines, another change that should be considered involves the radar source. The 4.3 GHz radar source performed as expected and was able to verify the operation of the short range, phased array system. However, since it was demonstrated that the reflections from the sand surface were difficult to detect, especially with the large noise signals present, a radar source operating at a higher frequency may be more suitable for imaging homogeneous sand surfaces. Since the scattering from a sand particle can be modeled as Rayleigh scattering, the scattered power is proportional to the fourth power of the frequency of the incident wave [21]. As a consequence, as the frequency is increased, the surface scattering becomes stronger and the loss as the waves propagate through the sand bed becomes greater. In addition, if the bandwidth of the radar source was also increased, better target discrimination could be achieved, and it may even be possible to probe beneath the surface to assemble a three-dimensional view of the dynamics occuring within the bed.

The general conclusion is that this system successfully demonstrated the operation of a phased-array imaging system, but, in its current state, it has limited use. Namely, it is limited to imaging surfaces having strong reflections and large surfaces changes. However, with modifications, it shows potential at becoming an accurate, high resolution, short range imaging system. Future work should continue to explore and implement improvements to the existing design to achieve this goal.

APPENDIX A: DERIVATION OF RADIATION PATTERN

The purpose of this appendix is to derive the radiation pattern for a circular antenna array. For a standard circular array, all antenna elements are oriented the same way, resulting in the derivation of the array's radiation pattern following directly from the pattern multiplication rule. This is the common approach for finding the radiation pattern of antenna arrays. If each antenna element is oriented differently in the plane, the usual derivation cannot be applied directly, but can be adapted by invoking the rotation property of the two-dimensional Fourier transform.

The derivation will proceed in several steps. First, to demonstrate the basic concepts, the radiation pattern of a uniform linear array will be derived. Extrapolating these ideas to two dimensions will yield the radiation pattern of the standard circular array (or any other planar array). Finally, the radiation pattern of a circular array with rotated elements will evolve from this last set of equations.

A.1 Radiation Pattern of a Linear Array

Consider a linear array of five rectangular apertures, all aligned on the x axis, with equal spacing between elements (Figure A.1). Applying superposition, the total radiated electric field is the sum of the electric fields produced by the elements.

The contribution of each element to the total electric field radiated by the array can be represented by a summation of individual fields [1]. Using Figure A.1 as an example, represent the far field electric field of element 0 by the vector $\mathbf{E}_0$. Because of path length differences to spatial locations, element 1 will produce an identical field pattern except for a phase shift,

$$\mathbf{E}_1 = \mathbf{E}_0 e^{jkd\sin\theta\cos\phi}.$$

(A.1)

Similarly the contributions from each of the other elements are

$$E_2 = E_0 e^{jk(2d)\sin\theta\cos\phi}$$

$$E_{-1} = E_0 e^{-jkd\sin\theta\cos\phi} \qquad \text{(A.2)}$$

$$E_{-2} = E_0 e^{-jk(2d)\sin\theta\cos\phi}$$

The total radiated electric field is the summation of individual fields:

$$E_T = E_{-2} + E_{-1} + E_0 + E_1 + E_2$$

$$= \sum_{n=-2}^{2} E_0 e^{jkx_n \sin\theta\cos\phi} \qquad \text{(A.3)}$$

where x_n is the x coordinate of the nth antenna element.
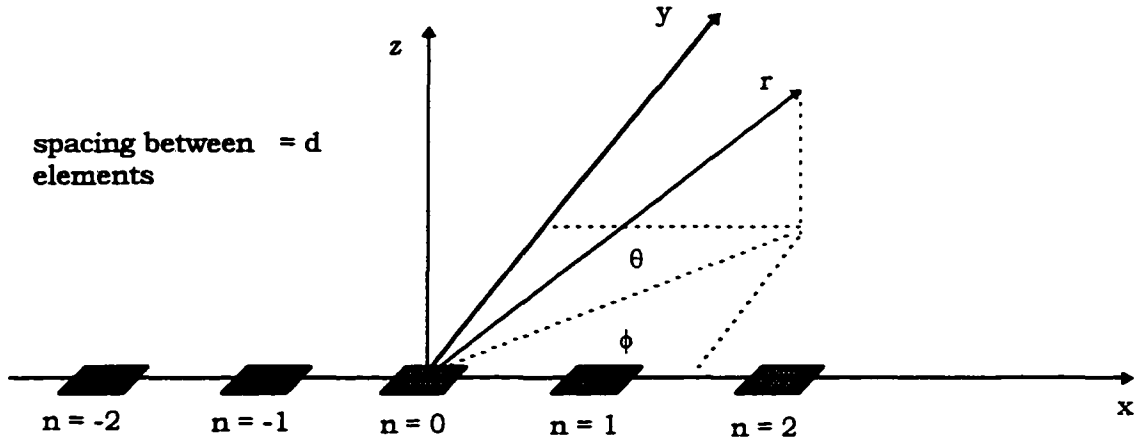
Figure A.1

The radiation pattern is the defined as the magnitude of the electric field [14]

$$E_T = |E_T| = \left| \sum_{n=-2}^{2} E_0 e^{jkx_n \sin\theta\cos\phi} \right| \qquad \text{(A.4)}$$

Eqn. (A.4) represents the radiation pattern of an antenna array that is either transmitting energy or receiving energy. (By reciprocity, the radiation pattern is identical for both cases.)

When the array operates as a transmitter and receiver simultaneously, Eqn. (A.4) is expanded to account for the various transmitter/receiver pairs and the different path lengths among them to a point in space,

$$|E_T| = \left| \sum_{n=-2}^{2} \sum_{x=-2}^{2} E_0 e^{jkx_n \sin\theta\cos\phi} e^{jkx_n \sin\theta\cos\phi} \right| \qquad \text{(A.5)}$$

where x_{tx} and x_{rx} are the x coordinates of the transmitting and receiving elements.

A.2 Radiation Pattern of a Circular Array

Shown in Figure A.2 is a circular antenna array with N identically oriented antenna elements equally spaced around the perimeter of the circle. The radiation pattern of the circular array is a twodimensional extension of the linear array. After adjusting the phase term, Eqn. (A.3) takes the form

$$\mathbf{E_T} = \sum_{n=1}^{9} \mathbf{E_0} e^{j(kx_n \sin\theta \cos\phi + ky_n \sin\theta \sin\phi)}$$

(A.6)

where x_n and y_n are the coordinate location of the antenna n. Similarly, the additional phase term can be incorporated into Eqn. (A.6) to produce the total radiation pattern of a circular array that is both transmitting and receiving energy.
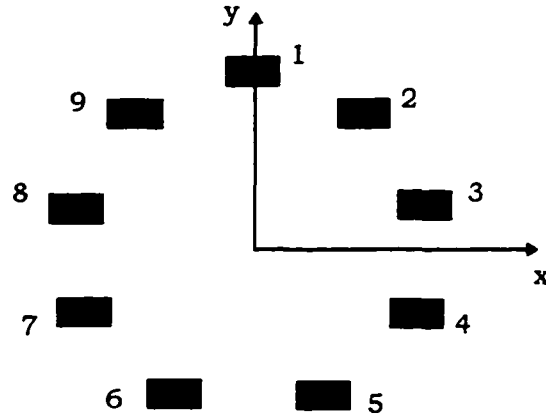
Figure A.2

A.3 Radiation Pattern of a Circular Array with Rotated Elements

Up until this point, no expression has been given for $\mathbf{E_0}$, the electric field pattern for a single array element. From antenna theory [14], the far field electric field pattern of an antenna is proportional to the two dimensional Fourier transform of the electric field at the surface of the aperture. It can be shown that the far electric field pattern of a rectangular aperture with dimensions a and b (Figure A.4) is

$$\mathbf{E}_0 = \left(\hat{\theta}\cos\theta\sin\phi + \hat{\phi}\cos\phi\right)jK\,\frac{e^{-jkr}}{4\pi r}\left\{\frac{\sin[k_y(\frac{b}{2})]}{k_y}\right\}\left\{\frac{\sin[(k_x + \frac{\pi}{a})\frac{a}{2}]}{k_x + \frac{\pi}{a}} + \frac{\sin[(k_x - \frac{\pi}{a})\frac{a}{2}]}{k_x - \frac{\pi}{a}}\right\} \qquad (A.7)$$

where j is the complex number $\sqrt{-1}$ and K represents a collection of constant terms.

According to the rotation property of Fourier transform theory, if the aperture is rotated an angle ϕ_0 about the z axis (Figure A.4), then the Fourier transform of the aperture will also rotate by an angle ϕ_0. Although the pattern multiplication rule no longer applies (due to ϕ_0 each element field may be different), the only modification to the standard circular array derivation is to replace ϕ by $\phi + \phi_0$ in the vector term of Eqn. (A.7). (The vector multiplication in the exponential term in Eqn. (A.6) will not be affected since this distance will remain the same regardless of the element rotation.)
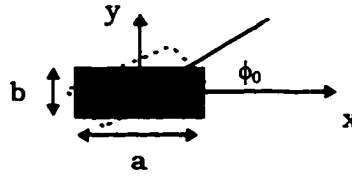
Figure A.4

Displayed in Figure A.5 is a nine element circular antenna array with each element aligned radially tangent.
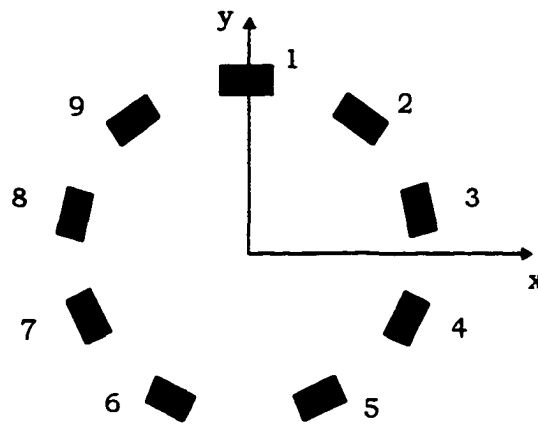
Figure A.5

In forming this array from the standard circular array of Figure A.4, each element was rotated, except element 1. The rotation angle for each element is tabulated in Table A.1. The far field radiation pattern of the array shown in Figure A.5 can be computed given this information, along with Eqns. (A.6) and (A.7)

Table A.1 Rotation angles for circular array elements

Element	1	2	3	4	5	6	7	8	9
Rotation Angle (deg.)	0	-40	-100	-120	-160	160	120	100	40

APPENDIX B: BEAMFORMER MATLAB MACRO

The signal processing algorithms were written as MATLAB version 4.0 macros. This appendix contains the code for the delay and sum beamforming algorithm. Comments begin with a percent sign.

```
%
% Surface Reconstruction using Delay and Sum Beamsteering
%
%       FMCW properties are used to calculate steering time delays. The near field beamformer
%equation governs the algorithm, but the array is focused on a plane located at a predefined
%average distance to the surface.
%
% Listing of some of the variables:
%       cosrc:      in-phase dataset, a matrix having (NTR*(NTR-1)/2) (rows) x (number of data
%                   samples)(cols)
%       sinrc:      quadrature dataset matrix
%       Npts:       Number of data samples per signal
%       fs:         Sampling frequency
%       NTR:        Number of antenna elements
%       dx, dy:     pixel dimensions
%       Diameter:   diameter of sand bed
%       FreqShift:  Cable shift frequency
%       zAve:       Average distance to surface
%       Npsd:       Number of points in FFT
%       w0:         2 * Pi * (Center frequency of FMCW radar source)
%       wSlope:     2*Pi* (chirp rate of FMCW radar source)
clear

% read antenna array element locations
antenna930c

% load data set, and process with noise reduction algorithms
bkgdsub

% load FMCW constants
constants

%% begin steering algorithm

% select pixel, determine its x, y coordinate location
for Index_x = 1: Npixels_x,
```

```
for Index_y = 1: Npixels_y,
     xdist = -Diameter/2 + dx * (Index_x - 0.5);
     ydist = -Diameter/2 + dy * (Index_y - 0.5);
     zFoc = zAve;

     Rxy  = sqrt(ydist^2 + xdist^2);        % Range to pixel
     Phi  = atan2(ydist , xdist);           % Direction to pixel
     Theta = atan2(Rxy, zAve);

     DelaySumOutput = zeros(1, Npts);       % initialize output of beamformer

     for tr = 1:NTR,                        % transmitter loop
                                            % determine tx/rx pair, 36 combinations
          AntSum = 0;
          for txm = 1: (tr - 1),
             AntSum = AntSum + NTR - txm;
          end;

          for rc = tr+1: NTR,               % receiver loop
             txrx = AntSum + (rc - tr);     % indices start at 1
```

% steering distances
%
```
          rm0tr = Ant_x(tr) * cos(Phi)*sin(Theta) + Ant_y(tr)* sin(Phi) * sin(Theta);
          rm0rc = Ant_x(rc) * cos(Phi)*sin(Theta) + Ant_y(rc)* sin(Phi) * sin(Theta);
```
% focusing term
```
          r0 = sqrt(xdist^2 + ydist^2 + zFoc^2);
          r2tr = (Ant_x(tr)^2 + Ant_y(tr)^2)/(r0^2);
          r2rc = (Ant_x(rc)^2 + Ant_y(rc)^2)/(r0^2);

          TxSteeringTimeDelay = (r0/c)*( 1 - sqrt(1 + r2tr - 2*r0*rm0tr /(r0^2)) );
          RxSteeringTimeDelay = (r0/c)*( 1 - sqrt(1 + r2rc - 2*r0*rm0rc /(r0^2)) );
          SteeringTimeDelay = TxSteeringTimeDelay + RxSteeringTimeDelay;
```

% estimated travel delay (negligible effect on calculations)
```
          Rrc = sqrt( ( Ant_y(rc) - ydist)^2 + ( Ant_x(rc) - xdist)^2 + zAve^2);
          Rtr = sqrt( ( Ant_y(tr) - ydist)^2 + ( Ant_x(tr) - xdist)^2 + zAve^2);
          RoundtripDelay = (Rtr + Rrc)/c;
```

% convert time delay to frequency and phase shifts
```
               wSteer = wSlope * SteeringTimeDelay;
               PhiSteer = (w0 - (1/2)*wSlope * SteeringTimeDelay) * SteeringTimeDelay - wSlope
                    * RoundtripDelay * SteeringTimeDelay;
```

% remove cable lengths from both in-phase and quadrature signals
```
               SignalCos = cosrc( txrx, : ) .* exp( j * 2 * pi * FreqShift * t);
               SignalSin = sinrc( txrx, : ) .* exp( j * 2 * pi * FreqShift * t);
```

% shift in-phase signal: cos(x) using the trig. identity cos(x + y) = cos(x)cos(y) - sin(x)sin(y)
% shift quadrature signal: sin(x) using the trig. identity sin(x + y) = sin(x)cos(y) + cos(x)sin(y)
```
               CosSignalShifted = SignalCos .* cos(wSteer * t + PhiSteer) - SignalSin .*
                    sin(wSteer * t + PhiSteer);
```

```
            SinSignalShifted = SignalSin .* cos(wSteer * t + PhiSteer) + SignalCos .*
                              sin(wSteer * t + PhiSteer);

% sum the delayed signals, account for the other equivalent antenna pair
            DelaySumOutput = DelaySumOutput + 2*(CosSignalShifted + j *
                              SinSignalShifted);


            end;  % rc loop
       end;    % tr loop


       FDelaySumOutput = fft(DelaySumOutput, Npsd);

% bandpass filter output if necessary
% determine dominant frequency
       [Amp, FreqIndex] = max(abs(FDelaySumOutput(1:2000)));
       FreqHat=(FreqIndex - 1) * fs/ Npsd;

% estimate range to surface
       R = FreqHat * c / Slope / 2;
% estimate power return from surface patch
       Amp = Amp^2

       xpts(Index_x, Index_y) = R * cos(Phi) * sin(Theta);       % surface matrices
       ypts(Index_x, Index_y) = R * sin(Phi) * sin(Theta);
       zpts(Index_x, Index_y) = R * cos(Theta);
       amplitude(Index_x, Index_y) = Amp;
   end;   % Index_x loop
end;      % Index_y loop

% convert from meters to feet
xfeet = xpts * 100.0 / (2.54 * 12);
yfeet = ypts * 100.0 / (2.54 * 12);
zfeet = zpts * 100.0 / (2.54 * 12);

% apply spatial filter
FltrSurf;
```

REFERENCES

[1]   Balanis, C.A. (1982). *Antenna Theory: Analysis and Design*, Harper & Row, New York.

[2]   Brown, W.M. and L.J. Porcello (1969). "An introduction to synthetic-aperture radar," *IEEE Spectrum*, vol. 6, pp. 52-62.

[3]   deRoos, A., J.J. Sinton, and P.T. Gough (1988). "The detection and classification of objects lying on the seafloor," *J. Acoust. Soc. Am.*, Vol. 84, No. 4, pp. 1456-76.

[4]   Dudgeon, D.E. (1977). "Fundamentals of digital array processing," *Proc. IEEE*, Vol. 65, No. 6, pp. 898-904.

[5]   Fasching, G.E., W.A. Loudin, and N. S. Smith (1994). "Capacitive system for three dimensional imaging of fluidized bed density," *IEEE Trans. Instr. and Meas.*, Vol. 43, No. 1, pp.56-62.

[6]   Fasching, G.E., *et al.* (c.1993). "Phased-array ultrasonic surface contour mapping system," Morgantown Energy Technology Center Draft Report, Morgantown, West Virginia.

[7]   Gonzalez, R.C. and R.E. Woods (1992). *Digital Image Processing*, Addison-Wesley, Reading, Massachusetts.

[8]   Gupta, I.G. (1994). "High resolution radar imaging using 2-D linear prediction," *IEEE Trans. Antennas Propagat.*, Vol. 42, No. 1, pp. 31-7.

[9]   Haykin, S. (1991). *Adaptive Filter Theory*, Prentice Hall, Englewood Cliffs, New Jersey.

[10] Jain, A.K. (1989). *Fundamentals of Image Processing*, Prentice Hall, Englewood Cliffs, New Jersey.

[11] Johnson, D.H. and D.E. Dudgeon (1993). *Array Signal Processing, Concepts and Techniques*, Prentice-Hall, Englewood Cliffs, New Jersey.

[12] Junk, K.W. (1993). "A model of coal combustion dynamics in a fluidized bed combustor," Ph.D. dissertation, Iowa State University, Ames, Iowa.

[13] Kirk, J.C., Jr. (1975). "A discussion of digital processing in synthetic aperture radar," *IEEE Trans. Aerospace And Electronic Systems*, Vol. AES-11, No. 3, pp.326-37.

[14] Kong, J.A. (1990). *Electromagnetic Wave Theory*, John Wiley and Sons, Inc., New York.

[15] Kunii, D. and O. Levenspiel (1991). *Fluidization Engineering*, Butterworth-Heinemann, Stoneham, Massachusetts.

[16] Kraus, J.D. (1988). *Antennas*, McGraw-Hill, New York.

[17] Munson, D.C., Jr., J. D. O'Brien, and W. K. Jenkins (1983). "A tomographic formulation of spotlight-mode synthetic aperture radar," *Proc. IEEE*, Vol. 71, No. 8, pp. 917-25.

[18] Olver, A.D. and L.G. Cuthbert (1988). "FMCW radar for hidden object detection," *IEE Proc. Part F*, Vol. 135, No. 4, pp. 354-61.

[19] Skolnik, M.L. (ed.)(1970). *Radar Handbook*, McGraw-Hill, New York.

[20] Smeenk, J. (1996). "The agglomeration of bed material during fluidized bed coal combustion", Master's thesis, Iowa State University, Ames, Iowa.

[21] Shen, L.C. and J.A. Kong (1987). *Applied Electromagnetism*, PWS Engineering, Boston, Massachusetts.

[22] Stove, A.G. (1992). "Linear FMCW radar techniques," *IEE Proc. Part F*, Vol. 139, No. 5, pp. 343-48.

[23] Stremler, F.M. (1992). *Introduction to Communication Systems*, Addison-Wesley, Reading, Massachusetts.

[24] Swingler, D.N. and R.S. Walker (1989). "Line-array beamforming using linear prediction for aperture interpolation and extrapolation," *IEEE Trans. Acoust., Speech, Signal Processing*, Vol. 37, No. 1, pp. 16-30.

[25] Tomiyasu, K. (1978). "Tutorial review of synthetic-aperture radar (SAR) with applications to imaging of the ocean surface," *Proc. IEEE*, Vol. 66, No. 5, pp. 563-83.

[26] Van Veen, B.D., and K.M. Buckley (1988). "Beamforming: A versatile approach to spatial filtering," *IEEE ASSP Mag.*, pp. 4-24.

[27] Vaugh, R.A. (ed.) (1990). *Microwave Remote Sensing for Oceanographic and Marine Weather-Forecast Models*, Kluwer Academic Publishers, Norwall, Massachusetts.

[28] Woods, G. S., D.L. Maskell, and M.V. Mahoney (1993). "A high accuracy microwave ranging system for industrial applications," *IEEE Trans. Instr. and Meas.*, Vol. 42, No. 4, pp. 812-16.